Continuum Mech. Thermodyn.
https://doi.org/10.1007/s00161-023-01252-6

S.I. : NON-CLASSICAL CONT MECH

Yadwinder Singh Joshan · Sushma Santapuri

Finite element modeling and analysis of flexoelectric plates using gradient electromechanical theory

Received: 19 December 2022 / Accepted: 12 August 2023

Abstract This work presents the development of a two-way coupled flexoelectric plate theory starting from a 3D gradient electromechanical theory. The gradient electromechanical theory considers three mechanical length scale parameters and two electric length scale parameters to account for both mechanical and electrical size effects. Variational formulation is used to derive the plate governing equations and boundary conditions considering Kirchhoff's assumptions. A computationally efficient C^2 continuous non-conforming finite element is developed to solve the resulting plate equations. To assess the accuracy of the non-conforming finite element framework, the results are compared with Navier-type analytical solution for a simply supported flexoelectric plate. The finite element framework is also validated with experimental results in the existing literature for a passive micro-plate. The results show excellent agreement with both analytical and experimental results. Furthermore, computational efficiency of the non-conforming element is compared with the standard conforming element, which contains greater degrees of freedom and continuity across all elemental edges. It was observed that the non-conforming element is almost twice as fast as the conforming element without a significant loss of accuracy. The 2D finite element formulation is subsequently used to analyze the size-dependent response of flexoelectric composite plates operating in both sensor and actuator modes. Various parametric studies are performed to analyze the effect of boundary conditions, length scale parameters, size of the plate, flexoelectric layer thickness ratio, etc., on the response of flexoelectric plate-type sensors and actuators. It is found that the effective electromechanical coupling increases in a flexoelectric plate at microscale (due to the size effects), and it is higher than standard piezoelectric materials for plate thickness $h \leq 8$ μm.

Keywords Flexoelectric plates · Finite element method · Non-conforming element · Strain gradient theory · Micro-sensors and actuators

1 Introduction

Direct flexoelectric effect is defined as spontaneous polarization observed in thin dielectric structures under applied strain gradient [1]. Conversely, these materials undergo deformation in the presence of electric field gradient [2]. This effect is observed in dielectric materials at micro- and nanoscales. Flexoelectric effect is often compared with the piezoelectric effect, which is found only in non-centrosymmetric dielectric crystals. Unlike the piezoelectric effect, flexoelectric effect can also occur in centro-symmetric dielectric materials [3]. Applied strain gradient breaks the charge symmetry of a flexoelectric crystal, resulting in a spontaneous polarization [2]. Furthermore, piezoelectric materials exhibit large electromechanical coupling at macro-scale, whereas flexoelectric effect is significant only in thin structures and is comparable to piezoelectric coupling at micro-/nanoscales [4,5]. Thus, flexoelectric materials are used as micro-transducers in MEMS and NEMS

Y. S. Joshan · S. Santapuri (✉)
Department of Applied Mechanics, Indian Institute of Technology Delhi, Hauz Khas, New Delhi 110016, India
E-mail: ssantapuri@am.iitd.ac.in

Published online: 09 September 2023

applications [6]. Specifically, they have been explored in applications such as micro-actuators [7,8], structural health monitoring [9], vibration control [10], curvature sensors [11], and energy harvesting [12].

Modeling of flexoelectric material-based structures and devices has been explored extensively in recent times [13–15]. The flexoelectric response of a dielectric material is dependent on the dimensions of the structure as the effect becomes significant only at smaller scales, i.e., at micro- and nanoscales [2,16,17]. Various size-dependent 3D continuum strain-gradient theories have been developed in the literature, wherein the mathematical form of the governing equations and boundary conditions are obtained using variational principle. Sahin and Dost [18] developed one of the earliest three-dimensional continuum flexoelectric theories, in which the independent electrical variables were polarization and polarization gradient, along with deformation gradient and its gradient as the mechanical variables. A linearized theory was also presented for infinitesimal strains and small polarization charges. Maranganti et al. [19] proposed a linear flexoelectric theory for centro-symmetric dielectrics considering free energy as a function of double deformation gradient and polarization. In this theory, two material length scale parameters were considered in the constitutive formulation for dilatational and rotational gradients. Majdoub et al. [3] presented a linear size-dependent piezo-flexoelectric theory for nanostructures. The authors used molecular dynamics to analyze a cantilever beam and observed that the effective electroelastic coefficient increases at nanoscale due to the size dependence of flexoelectric effect. In the above-mentioned continuum flexoelectric theories, along with some further developments [20–22], the focus of the study was on the modeling of direct flexoelectric effect and its applications. Converse flexoelectric effect is typically ignored as it is assumed to be insignificant compared to the direct effect. However, experimental studies by Abdollahi et al. [23] have shown that the converse flexoelectric effect may give rise to a large localized electroelastic response in all dielectric materials at micro-/nanoscales. They concluded that neglecting converse flexoelectricity may result in an incorrect estimation of piezoelectric coefficient using piezoresponse force microscopy. Moreover, analogous to the mechanical size effects which result in a stiffer material at microscale, recent studies have demonstrated an increase in the electrical permittivity of the material at smaller scales [17]. In order to observe these trends in the modeling of flexoelectric materials, Joshan and Santapuri [24] developed a two-way coupled gradient electromechanical theory for flexoelectric materials that incorporates both direct and converse flexoelectric effects. In this theory, three mechanical length scale parameters and two electrical length scale parameters were considered to model both mechanical and electric size effects. The theory was subsequently used to analyze curved flexoelectric beams.

Based on the polarization-strain gradient theories, one-dimensional beam models have been developed and have been extensively studied in the last decade. Yan and Jiang [5] developed an Euler–Bernoulli beam model for piezo-flexoelectric nanobeams. They analyzed the bending of flexoelectric nanobeams for different boundary conditions. Based on the Euler–Bernoulli flexoelectric beam model, Deng et al. [14] developed a flexoelectric theory for energy harvesting and found that the efficiency of the flexoelectric energy harvesters increases with a decrease in the sample size. This effect is also observed by Wang and Wang [25], and they found that the voltage output contributed by flexoelectric effect is five times higher than that by piezoelectric effect at the nanoscale. Yue et al. [26] developed Timoshenko beam model for bending and free vibration analysis of simply supported piezo-flexoelectric beams considering surface effects. In recent literature, beam models incorporating converse flexoelectricity have been developed [27–30]. Joshan and Santapuri [24] developed an electromechanically coupled C^2 continuous beam finite element model for curved flexoelectric beams considering both direct and converse flexoelectric effects.

Two-dimensional flexoelectric theories have also been an area of interest for researchers since MEMS- and NEMS-based actuator and sensor devices utilize thin patches of smart materials. As one of the earliest works in two-dimensional modeling of flexoelectric plates, Zhang et al. [31] presented classical plate theory (CLPT) to study the effect of flexoelectricity on bending analysis of piezoelectric nano-plates. They solved the governing equations for a clamped plate using Ritz method and found that flexoelectric effect is prominent in thinner plates of smaller sizes. Yang et al. [15] analyzed the bending and free vibration response of flexoelectric plates using CLPT. The Navier-type analytical solution was used to analyze the effect of thickness of plate on effective flexoelectric response. Li et al. [32] analyzed actuator response of a simply supported axisymmetric circular plate. The size effects were considered using strain gradient elasticity theory. Ebrahimi and Barati [33] used Eringen's non-local elasticity theory for vibration analysis of flexoelectric plates considering surface and thermal effects. Qi et al. [34] analyzed the size-dependent static and dynamic response of flexoelectric annular plate using strain gradient elasticity theory. Chen et al. [35] presented a CLPT energy harvester model for flexoelectric plates. Amir et al. [36] analyzed the effects of shear deformation on free vibration response of the flexoelectric sandwich plate using first-order shear deformation theory. These two-dimensional plate models are based on polarization-strain gradient flexoelectricity theory, i.e., free energy is considered to be a function

of polarization and strain gradient. However, compared to polarization, electric field is easier to control and measure in practical applications. Thus, electric field-strain gradient-based flexoelectric theories have recently been developed in the literature [37–39].

In the available literature, most of the existing flexoelectric plate models neglect converse flexoelectric effect. Only a few articles are available on plate theories considering converse flexoelectricity [40,41]. Moreover, most of these flexoelectric plate theories do not consider the electrical size effects that contribute to an increase in electric permittivity of the material at lower scales [17]. These effects were recently considered in Joshan and Santapuri [24] wherein a gradient electromechanical theory was developed for thin flexoelectric solids considering both direct and converse flexoelectric effects. This two-way coupled electromechanical theory is developed considering an electric field-based free energy function as they are easier to control and measure in sensor/actuator applications. This theory also incorporates both mechanical and electrical size effects.

In this work, a fully coupled flexoelectric plate theory is developed starting from the gradient electromechanical theory presented in Joshan and Santapuri [24]. A computationally efficient C^2 continuous non-conforming element is developed to solve the resulting 2D plate governing equations for different boundary and loading conditions. The theory is used to analyze flexoelectric composite plates consisting of active flexoelectric and passive (non-flexoelectric) layers operating in sensor and actuator modes. A combination of linear and quadratic terms is considered for modeling the variation of electrostatic potential across the thickness of the flexoelectric layer. Firstly, our finite element results are verified with Akgoz and Civalek [42] for the case of a passive micro-plate. Further, the flexoelectric plates are analyzed in two different modes: (1) sensor mode, wherein the electrostatic potential output is analyzed for flexoelectric plates under applied mechanical load, and (2) actuator mode, wherein the deformation of the flexoelectric plate is studied under applied electric potential. An analytical solution is also developed for simply supported plates to verify the accuracy of our finite element results. Our results for the non-conforming element were found to be 99.9% accurate in comparison with the analytical solution. Furthermore, computational efficiency of the non-conforming element is compared with the conforming element, and it is noted that the non-conforming element is 1.85 times faster than the conforming element. The conforming element is marginally more accurate as it contains greater degrees of freedom with C^2 continuity imposed on all elemental boundaries. Various parametric studies are performed to analyze the effect of boundary conditions, thickness of the plate, mechanical and electric length scale parameters on the sensor and actuator response of flexoelectric composite plates. The contribution of converse flexoelectricity in the response of a thin sensor for different thickness values of the flexoelectric plate is analyzed and is found to be around 20% of the total response. Application of our computationally efficient finite element framework towards the design of flexoelectric plate sensors and actuators is demonstrated through different examples.

2 Mathematical formulation

This section presents the development of a fully coupled flexoelectric plate theory starting from a 3D gradient electromechanical formulation. In addition to the mechanical size effects, this theory also considers the often neglected electrical size effects [17]. Recently, Joshan and Santapuri [24] developed a gradient electromechanical theory for thin beam structures considering both direct and converse flexoelectric effects. The two-way coupled electromechanical theory is developed considering a free energy function dependent on electric field and its gradient.

2.1 3D governing equations for a flexoelectric solid

In this section, a brief review of 3D governing equations and boundary conditions for a flexoelectric solid based on gradient electromechanical theory [24] is presented. The equilibrium governing equations and boundary conditions are derived using the principle of minimum potential energy. The expression for total potential energy in a flexoelectric solid is given by

$$\Pi = \int_{\mathcal{V}_0} \Omega(S_{ij}, G_{ijk}, E_i, K_{ij})\, \mathrm{d}V - \omega, \tag{1}$$

where $\mathcal{V}_0$ represents the total volume occupied by the flexoelectric solid, $\mathrm{d}V$ is the infinitesimal volume element, and ω denotes the work done by the externally applied mechanical and electric loads. The free energy function

Ω is expressed in terms of the infinitesimal strain tensor S_{ij}, strain gradient G_{ijk}, electric field E_i, and the electric field gradient K_{ij}. The infinitesimal strain tensor and its gradient are defined as:

$$S_{ij} = \frac{1}{2}(u_{i,j} + u_{j,i}), \quad G_{ijk} = S_{ij,k} = \frac{1}{2}(u_{i,jk} + u_{j,ik}), \tag{2}$$

where u_i represents the components of the mechanical displacement vector and $u_{i,j} = \partial u_i / \partial x_j$ denote the components of displacement gradient tensor. Similarly, the electric field vector E_i and electric field gradient tensor K_{ij} are given by:

$$E_i = -\phi_{,i}, \quad K_{ij} = E_{i,j} = -\phi_{,ij}, \tag{3}$$

where ϕ represents the scalar electrostatic potential. The governing equations are obtained by setting the first variation of potential energy (1) to zero, i.e.,

$$\delta\Pi = 0 \Rightarrow \int_{\mathcal{V}_0} \delta\Omega(S_{ij}, G_{ijk}, E_i, K_{ij})\, \mathrm{d}V - \delta\omega = 0, \tag{4}$$

where $\delta\Omega$ denotes the first variation of the free energy function given by [24]

$$\delta\Omega = T_{ij}\delta S_{ij} + H_{ijk}\delta G_{ijk} - D_i\delta E_i - B_{ij}\delta K_{ij}, \tag{5}$$

and

$$T_{ij} = \frac{\partial\Omega}{\partial S_{ij}}, \quad H_{ijk} = \frac{\partial\Omega}{\partial G_{ijk}}, \quad D_i = -\frac{\partial\Omega}{\partial E_i}, \quad B_{ij} = -\frac{\partial\Omega}{\partial K_{ij}}. \tag{6}$$

Here, D_i denotes the components of electric displacement vector and B_{ij} denotes the higher-order electric displacement tensor components; T_{ij} and H_{ijk} represent the Cartesian components of the Cauchy stress tensor and the higher-order stress tensor, respectively. The variation of free energy function $\delta\Omega$ can be expressed in terms of strain and electric potential variables using (2)– (3) as

$$\delta\Omega = T_{ij}\delta u_{i,j} + \hat{H}_{ijk}\delta u_{i,jk} + D_i\delta\phi_{,i} + B_{ij}\delta\phi_{,ij}, \tag{7}$$

where $\hat{H}_{ijk} = \frac{1}{2}(H_{ijk} + H_{jik})$. Finally, the first variation of the work done by external electroelastic loads, $\delta\omega$, is defined as

$$\delta\omega = \int_{\mathcal{V}_0} \left[f_i^b \delta u_i + \rho_v \delta\phi \right] \mathrm{d}V + \int_{\partial\mathcal{V}_0^t} t_i^a \delta u_i \, \mathrm{d}A + \int_{\partial\mathcal{V}_0^e} \rho_s \delta\phi \, \mathrm{d}A, \tag{8}$$

where $\partial\mathcal{V}_0^t$ represents a subset of the boundary $\partial\mathcal{V}_0$ on which the applied traction t_i^a is prescribed and $\partial\mathcal{V}_0^e$ represents the subset on which the surface charge density ρ_s is prescribed. Also, f_i^b represents the components of the body force and ρ_v denotes the applied volumetric charge density. The governing equations and boundary conditions are obtained by setting the first variation of potential energy to zero. The detailed derivation is discussed in Joshan et al. [24]. The 3D governing equations, applicable at every point within $\mathcal{V}_0$, are given by:

$$\delta u_i : \quad T_{ij,j} - \hat{H}_{ijk,jk} = -f_i^b, \tag{9}$$

$$\delta\phi : \quad D_{i,i} - B_{ij,ji} = -\rho_v. \tag{10}$$

The boundary conditions, specified at any point on $\partial\mathcal{V}_0$, may be prescribed in terms of applied traction/charges or displacement/electric potential and their derivatives as follows:

$$T_{ij}n_j - \hat{H}_{ijk,j}n_k + n_j n_k \hat{H}_{ijk}\, \Delta_p(n_p) - \Delta_k(n_j \hat{H}_{ijk}) = t_i^a \text{ or } u_i = u_i^* \text{ or } u_i^a, \tag{11}$$

$$\hat{H}_{ijk}n_j n_k = 0 \text{ or } u_i' = u_i'^*, \tag{12}$$

$$D_i n_i - B_{ij,j}n_i + n_j n_i B_{ij}\, \Delta_p(n_p) - \Delta_i(n_j B_{ij}) = \rho_s \text{ or } \phi = \phi^*, \tag{13}$$

$$B_{ij}n_i n_j = 0 \text{ or } \phi' = \phi'^*. \tag{14}$$

Here, n_i denotes the unit normal to the boundary surface $\partial\mathcal{V}_0$, $\Delta_j(\cdot)$ and $(\cdot)'$ denote the surface gradient and the normal gradient (derivative along the surface normal) operators, respectively, and the superscript * is

used to denote the specified fixed value of the quantity at the boundary. Finally, the edge boundary conditions, prescribed on the sharp edges of the boundary, are given by

$$[[n_j B_{ij} \overline{n}_i]] = 0 \text{ or } \phi = 0, \tag{15}$$

$$[[n_j \hat{H}_{ijk} \overline{n}_k]] = 0 \text{ or } u_i = 0, \tag{16}$$

where $\overline{n}_k$ is the surface unit vector normal to the edge and $[[\cdot]]$ denotes the jump in the value of the enclosed quantity across the sharp edge.

2.1.1 Linear constitutive model of an isotropic flexoelectric solid

The electroelastic free energy function Ω corresponding to a linear flexoelectric material considering both direct and converse flexoelectric effects is given by [24]

$$\begin{aligned}\Omega =& \frac{1}{2}(c_{ijkl} S_{ij} S_{kl} + g_{ijklmn} G_{ijk} G_{lmn} - \epsilon_{ij} E_i E_j - k_{ijkl} K_{ij} K_{kl}) - e_{ijk} E_i S_{jk} \\ & - f_{ijkl} E_i G_{jkl} - h_{ijkl} K_{ij} S_{kl},\end{aligned} \tag{17}$$

where c_{ijkl} represents the components of fourth-order stiffness tensor, g_{ijklmn} denotes higher-order stiffness tensor (relating strain gradient and higher-order stresses), ϵ_{ij} is the electric permittivity tensor, k_{ijkl} represents the higher-order electric permittivity tensor, e_{ijk} is the piezoelectric coupling tensor, f_{ijkl} is the direct flexoelectric coupling tensor and h_{ijkl} is the converse flexoelectric coupling tensor. The corresponding linear constitutive equations are obtained as follows [24]:

$$T_{ij} = \frac{\partial \Omega}{\partial S_{ij}} = c_{ijkl} S_{kl} - e_{ijk} E_k - h_{ijkl} K_{kl}, \tag{18}$$

$$H_{ijk} = \frac{\partial \Omega}{\partial G_{ijk}} = g_{ijklmn} G_{lmn} - f_{ijkl} E_l, \tag{19}$$

$$D_i = -\frac{\partial \Omega}{\partial E_i} = e_{ijk} S_{jk} + f_{ijkl} G_{jkl} + \epsilon_{ij} E_j, \tag{20}$$

$$B_{ij} = -\frac{\partial \Omega}{\partial K_{ij}} = k_{ijkl} K_{kl} + h_{ijkl} S_{kl}. \tag{21}$$

The linear constitutive equations (18)–(21) can be specialized to isotropic materials by reducing the material constants c_{ijkl}, g_{ijklmn}, ϵ_{ij}, k_{ijkl}, f_{ijkl}, and h_{ijkl} to their isotropic forms. The resulting isotropic equations are [24]:

$$T_{ij} = \lambda \delta_{ij} S_{kk} + 2\mu S_{ij} - h_1 \delta_{ij} K_{kk} - 2h_2 K_{ij}, \tag{22}$$

$$\begin{aligned}H_{ijk} =& 2a_1 \delta_{ij} G_{mmk} + \frac{1}{2} a_2 (2\delta_{ij} G_{kmm} + \delta_{ik} G_{mmj} + \delta_{jk} G_{mmi}) + a_3 (\delta_{jk} G_{imm} \\ & + \delta_{ik} G_{jmm}) + 2a_4 G_{ijk} + a_5 (G_{jki} + G_{kij}) - f_1 (\delta_{jk} E_i + \delta_{ik} E_j) - f_2 \delta_{ij} E_k,\end{aligned} \tag{23}$$

$$D_i = \epsilon E_i + 2f_1 G_{ijj} + f_2 G_{jji}, \tag{24}$$

$$B_{ij} = k_1 \delta_{ij} K_{kk} + 2k_2 K_{ij} + h_1 \delta_{ij} S_{kk} + 2h_2 S_{ij}, \tag{25}$$

where λ and μ denote elastic Lame's constants; a_i $(i = 1, 2, ...5)$ are the higher-order stiffness constants; ϵ denotes the dielectric material constant, k_1 and k_2 represent higher-order dielectric constants; f_1 and f_2 are coupling constants corresponding to direct flexoelectric effect; and h_1 and h_2 correspond to converse flexoelectric effect. The piezoelectric coupling tensor e_{ijk} vanishes for isotropic materials and in general for any material with a centrosymmetric crystal structure [43]. In the gradient electromechanical theory, the material constants a_i $(i = 1, 2, ..5)$ describing the relationship between higher-order stress and strain gradient (Eq. 23) are expressed as functions of characteristic length scale parameters l_0, l_1 and l_2 as follows:

$$\begin{aligned}&a_1 = \mu\Big(l_0^2 - \frac{1}{15} l_1^2 - \frac{1}{2} l_2^2\Big), \quad a_2 = \mu\Big(l_2^2 - \frac{4}{15} l_1^2\Big), \quad a_3 = \mu\Big(-\frac{4}{15} l_1^2 - \frac{1}{2} l_2^2\Big), \\ &a_4 = \mu\Big(\frac{1}{3} l_1^2 + l_2^2\Big), \quad a_5 = \mu\Big(\frac{2}{3} l_1^2 - l_2^2\Big),\end{aligned} \tag{26}$$

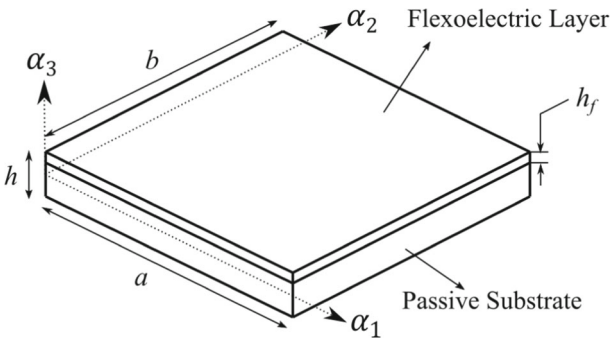

Fig. 1 Schematic of a composite flexoelectric plate consisting of a passive substrate and a flexoelectric layer of thickness h_f

These relationships were derived in Lam et al. [44] using the reduced form of constitutive equations for a linear elastic material (no electric field coupling), i.e.,

$$p_i = 2\mu l_0^2 \gamma_i, \quad \tau^1_{ijk} = 2\mu l_1^2 \eta^1_{ijk}, \quad m^s_{ij} = 2\mu l_2^2 \chi^s_{ij}, \tag{27}$$

where p_i, τ^1_{ijk} and m^s_{ij} are the work conjugates of the dilatation gradient vector γ_i, the deviatoric stretch tensor η^1_{ijk}, and the symmetric part of curvature tensor χ^s_{ij}, respectively. We note that there are several other possible formulations available in the literature to describe the length scale effects [19,45–50]. In this work, we consider two additional *electrical length scale parameters* l_0^e and l_1^e to describe the two higher-order dielectric constants k_1 and k_2 given by

$$k_1 = (l_0^e)^2 \epsilon, \quad k_2 = (l_1^e)^2 \epsilon, \tag{28}$$

where ϵ represents the dielectric permittivity of the material.

2.2 Modeling of flexoelectric composite plates

In what follows, a fully coupled classical plate theory is presented for the analysis of flexoelectric composite plates. A rectangular flexoelectric plate consisting of passive (non-flexoelectric) and flexoelectric layers is modeled in Cartesian coordinate system $(\alpha_1, \alpha_2, \alpha_3)$ as shown in Fig. 1. The coordinate α_3 is along the thickness of plate and normal to the mid-plane $\mathcal{A}_0$ at $\alpha_3 = 0$. Two-dimensional coordinates (α_1, α_2) are used to define the position of any point on $\mathcal{A}_0$. The dimensions of flexoelectric plate along α_1 and α_2 directions are taken as a and b, respectively. Total thickness of the plate and the thickness of the flexoelectric layer are denoted by h and h_f, respectively.

Displacement field variation: The flexoelectric composite plate is modeled using the classical plate theory (CLPT) [31,51]. CLPT is the simplest two-dimensional plate theory based on Kirchhoff assumptions and is suitable for analysis of thin plates. This theory does not consider transverse shear and normal stresses, which are assumed to be negligible compared to in-plane normal and shear stresses in thin structures [52,53]. The displacement vector u_i of any point $(\alpha_1, \alpha_2, \alpha_3)$ on the plate is given by [51]:

$$u_1(\alpha_1, \alpha_2, \alpha_3) = u_0(\alpha_1, \alpha_2) - \alpha_3 \frac{\partial w_0(\alpha_1, \alpha_2)}{\partial \alpha_1}, \tag{29}$$

$$u_2(\alpha_1, \alpha_2, \alpha_3) = v_0(\alpha_1, \alpha_2) - \alpha_3 \frac{\partial w_0(\alpha_1, \alpha_2)}{\partial \alpha_2}, \tag{30}$$

$$u_3(\alpha_1, \alpha_2, \alpha_3) = w_0(\alpha_1, \alpha_2), \tag{31}$$

where u_0, v_0 and w_0 are the displacements at the mid-plane along α_1, α_2 and α_3 directions, respectively. The infinitesimal strain components S_{ij} are obtained by substituting (29)–(31) in $(2)_1$ as

$$S_{11} = \frac{\partial u_1}{\partial \alpha_1} = \frac{\partial u_0}{\partial \alpha_1} - \alpha_3 \frac{\partial^2 w_0}{\partial \alpha_1^2}, \quad S_{22} = \frac{\partial u_2}{\partial \alpha_2} = \frac{\partial v_0}{\partial \alpha_2} - \alpha_3 \frac{\partial^2 w_0}{\partial \alpha_2^2}, \tag{32}$$

$$S_{12} = S_{21} = \frac{1}{2}\left(\frac{\partial u_1}{\partial \alpha_2} + \frac{\partial u_2}{\partial \alpha_1}\right) = \frac{1}{2}\left(\frac{\partial u_0}{\partial \alpha_2} + \frac{\partial v_0}{\partial \alpha_1} - 2\alpha_3 \frac{\partial^2 w_0}{\partial \alpha_1 \partial \alpha_2}\right), \tag{33}$$

$$S_{33} = \frac{\partial u_3}{\partial \alpha_3} = 0, \quad S_{32} = S_{23} = \frac{1}{2}\left(\frac{\partial u_3}{\partial \alpha_2} + \frac{\partial u_2}{\partial \alpha_3}\right) = 0, \quad S_{31} = S_{13} = \frac{1}{2}\left(\frac{\partial u_3}{\partial \alpha_1} + \frac{\partial u_1}{\partial \alpha_3}\right) = 0. \tag{34}$$

The corresponding nonzero strain gradients are obtained using Eq. $(2)_2$, as

$$G_{111} = \frac{\partial^2 u_0}{\partial \alpha_1^2} - \alpha_3 \frac{\partial^3 w_0}{\partial \alpha_1^3}, \quad G_{112} = \frac{\partial^2 u_0}{\partial \alpha_1 \partial \alpha_2} - \alpha_3 \frac{\partial^3 w_0}{\partial \alpha_1^2 \partial \alpha_2}, \quad G_{113} = -\frac{\partial^2 w_0}{\partial \alpha_1^2}, \tag{35}$$

$$G_{221} = \frac{\partial^2 v_0}{\partial \alpha_2 \partial \alpha_1} - \alpha_3 \frac{\partial^3 w_0}{\partial \alpha_2^2 \partial \alpha_1}, \quad G_{222} = \frac{\partial^2 v_0}{\partial \alpha_2^2} - \alpha_3 \frac{\partial^3 w_0}{\partial \alpha_2^3}, \quad G_{223} = -\frac{\partial^2 w_0}{\partial \alpha_2^2}, \tag{36}$$

$$G_{121} = G_{211} = \frac{1}{2}\left(\frac{\partial^2 u_0}{\partial \alpha_2 \partial \alpha_1} + \frac{\partial^2 v_0}{\partial \alpha_1^2} - 2\alpha_3 \frac{\partial^3 w_0}{\partial \alpha_1^2 \partial \alpha_2}\right), \tag{37}$$

$$G_{122} = G_{212} = \frac{1}{2}\left(\frac{\partial^2 u_0}{\partial \alpha_2^2} + \frac{\partial^2 v_0}{\partial \alpha_1 \partial \alpha_2} - 2\alpha_3 \frac{\partial^3 w_0}{\partial \alpha_1 \partial \alpha_2^2}\right), \tag{38}$$

$$G_{123} = G_{213} = -\frac{\partial^2 w_0}{\partial \alpha_1 \partial \alpha_2}. \tag{39}$$

Electric potential variation: The electrostatic potential is often assumed to be linearly varying across the thickness of the flexoelectric structures [2,54,55]. However, higher-order correction terms can be incorporated for a more accurate model, especially in the sensor mode [56]. These higher-order terms are modeled as quadratic or other non-polynomial functions in the literature [57,58]. In the present formulation, a quadratic variation of electrostatic potential ϕ is assumed across the thickness of flexoelectric layer as follows:

$$\phi(\alpha_1, \alpha_2, \alpha_3) = g_0(\alpha_3)\phi_0(\alpha_1, \alpha_2) + g_1(\alpha_3)\phi_1(\alpha_1, \alpha_2) \quad \alpha^l \le \alpha_3 \le \alpha^u, \tag{40}$$

where ϕ_0 is potential on the top surface of the flexoelectric layer (equal to the potential difference applied across the layer in actuator mode), ϕ_1 is the higher-order correction term, α^u and α^l are the thickness coordinates of the top and bottom surface of the flexoelectric layer. The linear function $g_0(\alpha_3)$ and quadratic function $g_1(\alpha_3)$ are defined as:

$$g_0(\alpha_3) = \frac{\alpha_3 - \alpha^l}{\alpha^u - \alpha^l}, \quad g_1(\alpha_3) = -\frac{4(\alpha^l - \alpha_3)(\alpha^u - \alpha_3)}{(h_f)^2}. \tag{41}$$

Components of electric field and its gradient can now be obtained using (3) as:

$$E_1 = -\frac{\partial \phi}{\partial \alpha_1} = -g_1 \frac{\partial \phi_1}{\partial \alpha_1} - g_0 \frac{\partial \phi_0}{\partial \alpha_1}, \tag{42}$$

$$E_2 = -\frac{\partial \phi}{\partial \alpha_2} = -g_1 \frac{\partial \phi_1}{\partial \alpha_2} - g_0 \frac{\partial \phi_0}{\partial \alpha_2}, \tag{43}$$

$$E_3 = -\frac{\partial \phi}{\partial \alpha_3} = -g_1' \phi_1 - g_0' \phi_0, \tag{44}$$

and

$$K_{11} = \frac{\partial E_1}{\partial \alpha_1} = -g_1 \frac{\partial^2 \phi_1}{\partial \alpha_1^2} - g_0 \frac{\partial^2 \phi_0}{\partial \alpha_1^2}, \tag{45}$$

$$K_{22} = \frac{\partial E_2}{\partial \alpha_2} = -g_1 \frac{\partial^2 \phi_1}{\partial \alpha_2^2} - g_0 \frac{\partial^2 \phi_0}{\partial \alpha_2^2}, \tag{46}$$

$$K_{12} = K_{21} = \frac{\partial E_1}{\partial \alpha_2} = -g_1 \frac{\partial^2 \phi_1}{\partial \alpha_1 \partial \alpha_2} - g_0 \frac{\partial^2 \phi_0}{\partial \alpha_1 \partial \alpha_2} \tag{47}$$

$$K_{13} = K_{31} = \frac{\partial E_1}{\partial \alpha_3} = -g_1' \frac{\partial \phi_1}{\partial \alpha_1} - g_0' \frac{\partial \phi_0}{\partial \alpha_1} \tag{48}$$

$$K_{23} = K_{32} = \frac{\partial E_2}{\partial \alpha_3} = -g_1' \frac{\partial \phi_1}{\partial \alpha_2} - g_0' \frac{\partial \phi_0}{\partial \alpha_2} \tag{49}$$

$$K_{33} = \frac{\partial E_3}{\partial \alpha_3} = -g_1'' \phi_1 - g_0'' \phi_0. \tag{50}$$

where $(\cdot)'$ denotes the derivative of the function with respect to α_3.

2D constitutive equations: The three-dimensional constitutive equations (22)–(25) are reduced to 2D form for composite flexoelectric plates as follows:

$$\overline{\mathbf{T}}_{\{3\times1\}} = \overline{\mathbf{Q}}^{\mathbf{c}}_{\{3\times3\}} \overline{\mathbf{S}}_{\{3\times1\}} - \overline{\mathbf{h}}_{\{3\times6\}} \overline{\mathbf{K}}_{\{6\times1\}}, \tag{51}$$

$$\overline{\mathbf{H}}_{\{9\times1\}} = \overline{\mathbf{Q}}^{\mathbf{g}}_{\{9\times9\}} \overline{\mathbf{G}}_{\{9\times1\}} - \overline{\mathbf{f}}_{\{9\times3\}} \overline{\mathbf{E}}_{\{3\times1\}}, \tag{52}$$

$$\overline{\mathbf{D}}_{\{3\times1\}} = \overline{\boldsymbol{\epsilon}}_{\{3\times3\}} \overline{\mathbf{E}}_{\{3\times1\}} + \overline{\mathbf{f}}^{\mathrm{T}}_{\{3\times9\}} \overline{\mathbf{G}}_{\{9\times1\}}, \tag{53}$$

$$\overline{\mathbf{B}}_{\{6\times1\}} = \overline{\mathbf{k}}_{\{6\times6\}} \overline{\mathbf{K}}_{\{6\times1\}} + \overline{\mathbf{h}}^{\mathrm{T}}_{\{6\times3\}} \overline{\mathbf{S}}_{\{3\times1\}}, \tag{54}$$

where the column matrices $\overline{\mathbf{T}} = \begin{bmatrix} T_{11} & T_{22} & T_{12} \end{bmatrix}^{\mathrm{T}}$ and $\overline{\mathbf{S}} = \begin{bmatrix} S_{11} & S_{22} & S_{12} \end{bmatrix}^{\mathrm{T}}$ denote the independent components of 2D stress and strain tensors, respectively. Similarly, $\overline{\mathbf{H}}$, $\overline{\mathbf{G}}$, $\overline{\mathbf{D}}$, $\overline{\mathbf{E}}$, $\overline{\mathbf{B}}$ and $\overline{\mathbf{K}}$ denote matrices consisting of 2D components of higher-order stress, strain gradient, electric displacement, electric field, higher-order electric displacement and electric field gradient, respectively. The components of these matrices are listed in "Appendix A". The quantities $\overline{\mathbf{Q}}^{\mathbf{c}}$, $\overline{\mathbf{Q}}^{\mathbf{g}}$, $\overline{\boldsymbol{\epsilon}}$, $\overline{\mathbf{k}}$, $\overline{\mathbf{h}}$ and $\overline{\mathbf{f}}$ denote the 2D material constants, namely the stiffness matrix, higher-order stiffness matrix, permittivity matrix, higher-order permittivity matrix, converse flexoelectric coefficient matrix and direct flexoelectric coefficient matrix, respectively. The components of these matrices are also listed in Appendix A.

2.3 Formulation of flexoelectric plate theory

In what follows, the derivation of 2D governing equations for a flexoelectric plate under transverse electromechanical loading is presented by starting from the potential energy expression (1). The first variation of work done due to externally applied electromechanical loads can be expressed in the form

$$\delta\omega = \int_0^a \int_0^b t_3^a \delta u_3 \, \mathrm{d}\alpha_2 \mathrm{d}\alpha_1 + \int_0^a \int_0^b \rho_s \delta\phi_0 \, \mathrm{d}\alpha_2 \mathrm{d}\alpha_1, \tag{55}$$

where t_3^a represents the resultant traction along the transverse direction on the top and bottom surfaces ($\alpha_3 = \pm h/2$), and ρ_s denotes the surface charge density applied on the top surface ($\alpha_3 = h/2$) of the flexoelectric layer. The volumetric charge density and mechanical body force terms have not been included in our analysis. However, Eq. (55) may be easily modified to incorporate these terms. For thin plate structures, the traction components are expressed in terms of applied transverse load as follows:

$$\int_0^a \int_0^b t_3^a \, \mathrm{d}\alpha_2 \mathrm{d}\alpha_1 = \int_0^a \int_0^b [q_3^+(\alpha_1, \alpha_2) + q_3^-(\alpha_1, \alpha_2)] \, \mathrm{d}\alpha_2 \mathrm{d}\alpha_1 = \int_0^a \int_0^b q_3(\alpha_1, \alpha_2) \, \mathrm{d}\alpha_2 \mathrm{d}\alpha_1, \tag{56}$$

where q_3^+ and q_3^- are transverse loads per unit area acting on the top and bottom surfaces of the plate and $q_3 = q_3^+ + q_3^-$ is the resultant transverse load per unit area of the plate. The plate governing equations are now obtained by substituting nonzero strain and strain gradient components (32)–(39) and the electric field and electric field gradient components (42)–(50) into Eq. (5) and integrating across the plate thickness α_3 as follows:

$$\begin{aligned} \int_{\mathcal{V}_0} \delta\Omega \mathrm{d}V &= \int_{\mathcal{A}_0} \int_{\alpha_3=-\frac{h}{2}}^{\alpha_3=\frac{h}{2}} \delta\Omega \, \mathrm{d}V \\ &= \int_{\mathcal{A}_0} \left[N_{11} \frac{\partial \delta u_0}{\partial \alpha_1} - M_{11} \frac{\partial^2 \delta w_0}{\partial \alpha_1^2} + N_{22} \frac{\partial \delta v_0}{\partial \alpha_2} - M_{22} \frac{\partial^2 \delta w_0}{\partial \alpha_2^2} + N_{12} \left(\frac{\partial \delta u_0}{\partial \alpha_2} + \frac{\partial \delta v_0}{\partial \alpha_1} \right) \right. \end{aligned}$$

$$
\begin{aligned}
&- 2M_{12}\frac{\partial^2\delta w_0}{\partial\alpha_1\partial\alpha_2} + N^h_{111}\frac{\partial^2\delta u_0}{\partial\alpha_1^2} - M^h_{111}\frac{\partial^3\delta w_0}{\partial\alpha_1^3} + N^h_{112}\frac{\partial^2\delta u_0}{\partial\alpha_1\partial\alpha_2} - M^h_{112}\frac{\partial^3\delta w_0}{\partial\alpha_1^2\partial\alpha_2}\\
&- N^h_{113}\frac{\partial^2\delta w_0}{\partial\alpha_1^2} + N^h_{221}\frac{\partial^2\delta v_0}{\partial\alpha_2\partial\alpha_1} - M^h_{221}\frac{\partial^3\delta w_0}{\partial\alpha_2^2\partial\alpha_1} + N^h_{222}\frac{\partial^2\delta v_0}{\partial\alpha_2^2} - M^h_{222}\frac{\partial^3\delta w_0}{\partial\alpha_2^3}\\
&- N^h_{223}\frac{\partial^2\delta w_0}{\partial\alpha_2^2} + N^h_{121}\left(\frac{\partial^2\delta u_0}{\partial\alpha_2\partial\alpha_1} + \frac{\partial^2\delta v_0}{\partial\alpha_1^2}\right) - 2M^h_{121}\frac{\partial^3\delta w_0}{\partial\alpha_1^2\partial\alpha_2}\\
&+ N^h_{122}\left(\frac{\partial^2\delta u_0}{\partial\alpha_2^2} + \frac{\partial^2\delta v_0}{\partial\alpha_1\partial\alpha_2}\right) - 2M^h_{122}\frac{\partial^3\delta w_0}{\partial\alpha_1\partial\alpha_2^2} - 2N^h_{123}\frac{\partial^2\delta w_0}{\partial\alpha_1\partial\alpha_2}\\
&+ D^g_1\frac{\partial\delta\phi_1}{\partial\alpha_1} + D^g_2\frac{\partial\delta\phi_1}{\partial\alpha_2} + D^{g'}_3\delta\phi_1 + B^g_{11}\frac{\partial^2\delta\phi_1}{\partial\alpha_1^2} + B^g_{22}\frac{\partial^2\delta\phi_1}{\partial\alpha_2^2} + B^{g''}_{33}\delta\phi_1\\
&+ 2B^g_{12}\frac{\partial^2\delta\phi_1}{\partial\alpha_1\partial\alpha_2} + 2B^{g'}_{13}\frac{\partial\delta\phi_1}{\partial\alpha_1} + 2B^{g'}_{23}\frac{\partial\delta\phi_1}{\partial\alpha_2} + D^a_1\frac{\partial\delta\phi_0}{\partial\alpha_1} + D^a_2\frac{\partial\delta\phi_0}{\partial\alpha_2} + D^{a'}_3\delta\phi_0\\
&+ B^a_{11}\frac{\partial^2\delta\phi_0}{\partial\alpha_1^2} + B^a_{22}\frac{\partial^2\delta\phi_0}{\partial\alpha_2^2} + B^{a''}_{33}\delta\phi_0 + 2B^a_{12}\frac{\partial^2\delta\phi_0}{\partial\alpha_1\partial\alpha_2} + 2B^{a'}_{13}\frac{\partial\delta\phi_0}{\partial\alpha_1}\\
&+ 2B^{a'}_{23}\frac{\partial\delta\phi_0}{\partial\alpha_2}\Bigg]\mathrm{d}\alpha_2\mathrm{d}\alpha_1,
\end{aligned}
\tag{57}
$$

where $\mathcal{A}_0$ represents the area of the mid-plane ($\alpha_3 = 0$) of flexoelectric plate. Also, the stress resultants N, moment resultants M, higher-order stress resultants N^h, higher-order moment resultants M^h, charge displacement resultants D^g, $D^{g'}$, D^a, $D^{a'}$, and higher-order charge displacement resultants B^g, $B^{g'}$, $B^{g''}$, B^a, $B^{a'}$, $B^{a''}$ are defined as follows:

$$
\begin{bmatrix} N_{11} & N_{22} & N_{12} \\ N^h_{111} & N^h_{221} & N^h_{121} \\ N^h_{112} & N^h_{222} & N^h_{122} \\ N^h_{113} & N^h_{223} & N^h_{123} \end{bmatrix} = \int_{-\frac{h}{2}}^{\frac{h}{2}} \begin{bmatrix} T_{11} & T_{22} & T_{12} \\ H_{111} & H_{221} & H_{121} \\ H_{112} & H_{222} & H_{122} \\ H_{113} & H_{223} & H_{123} \end{bmatrix} \mathrm{d}\alpha_3, \tag{58}
$$

$$
\begin{bmatrix} M_{11} & M_{22} & M_{12} \\ M^h_{111} & M^h_{221} & M^h_{121} \\ M^h_{112} & M^h_{222} & M^h_{122} \end{bmatrix} = \int_{-\frac{h}{2}}^{\frac{h}{2}} \alpha_3 \begin{bmatrix} T_{11} & T_{22} & T_{12} \\ H_{111} & H_{221} & H_{121} \\ H_{112} & H_{222} & H_{122} \end{bmatrix} \mathrm{d}\alpha_3, \tag{59}
$$

$$
\begin{bmatrix} D^g_1 \\ D^g_2 \\ D^{g'}_3 \end{bmatrix} = \int_{-\frac{h}{2}}^{\frac{h}{2}} \begin{bmatrix} g_1(\alpha_3)D_1 \\ g_1(\alpha_3)D_2 \\ g_1'(\alpha_3)D_3 \end{bmatrix} \mathrm{d}\alpha_3, \quad \begin{bmatrix} D^a_1 \\ D^a_2 \\ D^{a'}_3 \end{bmatrix} = \int_{-\frac{h}{2}}^{\frac{h}{2}} \begin{bmatrix} g_0(\alpha_3)D_1 \\ g_0(\alpha_3)D_2 \\ g_0'(\alpha_3)D_3 \end{bmatrix} \mathrm{d}\alpha_3, \tag{60}
$$

$$
\begin{bmatrix} B^g_{11} & B^g_{12} & B^a_{11} & B^a_{12} \\ B^g_{22} & B^{g'}_{13} & B^a_{22} & B^{a'}_{13} \\ B^{g''}_{33} & B^{g'}_{23} & B^{a''}_{33} & B^{a'}_{23} \end{bmatrix} = \int_{-\frac{h}{2}}^{\frac{h}{2}} \begin{bmatrix} g_1(\alpha_3)B_{11} & g_1(\alpha_3)B_{12} & g_0(\alpha_3)B_{11} & g_0(\alpha_3)B_{12} \\ g_1(\alpha_3)B_{22} & g_1'(\alpha_3)B_{13} & g_0(\alpha_3)B_{22} & g_0'(\alpha_3)B_{13} \\ g_1''(\alpha_3)B_{33} & g_1'(\alpha_3)B_{23} & g_0''(\alpha_3)B_{33} & g_0'(\alpha_3)B_{23} \end{bmatrix} \mathrm{d}\alpha_3. \tag{61}
$$

Equation (57) is further reduced using integration by parts and reduced to strong form. The terms corresponding to variation of independent variables (δu_0, δv_0, δw_0, $\delta\phi_1$, $\delta\phi_0$) are grouped, and the governing equations are obtained using the fundamental lemma of variation [59]. As δu_0, δv_0, δw_0, $\delta\phi_1$ and $\delta\phi_0$ are arbitrary, the

governing equations can be obtained equating their coefficients in the energy expression to zero. The Euler–Lagrange equations for the classical flexoelectric plate are thus obtained, given as follows:

$$u_0: \quad -\frac{\partial N_{11}}{\partial \alpha_1}-\frac{\partial N_{12}}{\partial \alpha_2}+\frac{\partial^2 N^h_{111}}{\partial \alpha_1^2}+\frac{\partial^2 N^h_{112}}{\partial \alpha_1 \partial \alpha_2}+\frac{\partial^2 N^h_{121}}{\partial \alpha_2 \partial \alpha_1}+\frac{\partial^2 N^h_{122}}{\partial \alpha_2^2}=0, \tag{62}$$

$$v_0: \quad -\frac{\partial N_{22}}{\partial \alpha_2}-\frac{\partial N_{12}}{\partial \alpha_1}+\frac{\partial^2 N^h_{221}}{\partial \alpha_2 \partial \alpha_1}+\frac{\partial^2 N^h_{222}}{\partial \alpha_2^2}+\frac{\partial^2 N^h_{121}}{\partial \alpha_1^2}+\frac{\partial^2 N^h_{122}}{\partial \alpha_1 \partial \alpha_2}=0, \tag{63}$$

$$\begin{aligned} w_0: \quad & -\frac{\partial^2 M_{11}}{\partial \alpha_1^2}-\frac{\partial^2 M_{22}}{\partial \alpha_2^2}-2\frac{\partial^2 M_{12}}{\partial \alpha_1 \partial \alpha_2}+\frac{\partial^3 M^h_{111}}{\partial \alpha_1^3}+\frac{\partial^3 M^h_{112}}{\partial \alpha_1^2 \partial \alpha_2}-\frac{\partial^2 N^h_{113}}{\partial \alpha_1^2}+\frac{\partial^3 M^h_{221}}{\partial \alpha_2^2 \partial \alpha_1} \\ & +\frac{\partial^3 M^h_{222}}{\partial \alpha_2^3}-\frac{\partial^2 N^h_{223}}{\partial \alpha_2^2}+2\frac{\partial^3 M^h_{121}}{\partial \alpha_1^2 \partial \alpha_2}+2\frac{\partial^3 M^h_{122}}{\partial \alpha_1 \partial \alpha_2^2}-2\frac{\partial^2 N^h_{123}}{\partial \alpha_1 \partial \alpha_2}=q, \end{aligned} \tag{64}$$

$$\phi_1: \quad -\frac{\partial D^g_1}{\partial \alpha_1}-\frac{\partial D^g_2}{\partial \alpha_2}+D^{g'}_3+\frac{\partial^2 B^g_{11}}{\partial \alpha_1^2}+\frac{\partial^2 B^g_{22}}{\partial \alpha_2^2}+B^{g''}_{33}+2\frac{\partial^2 B^g_{12}}{\partial \alpha_1 \partial \alpha_2}-2\frac{\partial B^{g'}_{13}}{\partial \alpha_1}-2\frac{\partial B^{g'}_{23}}{\partial \alpha_2}=0, \tag{65}$$

$$\phi_0: \quad -\frac{\partial D^a_1}{\partial \alpha_1}-\frac{\partial D^a_2}{\partial \alpha_2}+D^{a'}_3+\frac{\partial^2 B^a_{11}}{\partial \alpha_1^2}+\frac{\partial^2 B^a_{22}}{\partial \alpha_2^2}+B^{a''}_{33}+2\frac{\partial^2 B^a_{12}}{\partial \alpha_1 \partial \alpha_2}-2\frac{\partial B^{a'}_{13}}{\partial \alpha_1}-2\frac{\partial B^{a'}_{23}}{\partial \alpha_2}=0. \tag{66}$$

The corresponding natural and essential boundary conditions on the four edges of the plate are given by

On edges $\alpha_1 = 0$ and $\alpha_1 = a$

$$\text{either } u_0 = u_0^* \text{ or } N_{11}-\frac{\partial N^h_{111}}{\partial \alpha_1}-\frac{\partial N^h_{112}}{\partial \alpha_2}-\frac{\partial N^h_{121}}{\partial \alpha_2}=0, \quad \text{either } \frac{\partial u_0}{\partial \alpha_1}=\frac{\partial u_0^*}{\partial \alpha_1} \text{ or } N^h_{111}=0,$$

$$\text{either } w_0 = w_0^* \text{ or } \frac{\partial M_{11}}{\partial \alpha_1}+2\frac{\partial M_{12}}{\partial \alpha_2}-\frac{\partial^2 M^h_{111}}{\partial \alpha_1^2}-\frac{\partial^2 M^h_{112}}{\partial \alpha_2 \partial \alpha_1}+\frac{\partial N^h_{113}}{\partial \alpha_1}-2\frac{\partial^2 M^h_{121}}{\partial \alpha_1 \partial \alpha_2}+2\frac{\partial N^h_{123}}{\partial \alpha_2}=0,$$

$$\text{either } \frac{\partial w_0}{\partial \alpha_1}=\frac{\partial w_0^*}{\partial \alpha_1} \text{ or } -M_{11}+\frac{\partial M^h_{111}}{\partial \alpha_1}+\frac{\partial M^h_{112}}{\partial \alpha_2}-N^h_{113}+2\frac{\partial M^h_{121}}{\partial \alpha_2}=0,$$

$$\text{either } \frac{\partial w_0}{\partial \alpha_2}=\frac{\partial w_0^*}{\partial \alpha_2} \text{ or } \frac{\partial M^h_{221}}{\partial \alpha_2}+2\frac{\partial M^h_{122}}{\partial \alpha_2}=0, \quad \text{either } \frac{\partial^2 w_0}{\partial \alpha_1^2}=\frac{\partial^2 w_0^*}{\partial \alpha_1^2} \text{ or } M^h_{111}=0,$$

$$\text{either } v_0 = v_0^* \text{ or } N_{12}-\frac{\partial N^h_{221}}{\partial \alpha_2}-\frac{\partial N^h_{121}}{\partial \alpha_1}-\frac{\partial N^h_{122}}{\partial \alpha_2}=0, \quad \text{either } \frac{\partial v_0}{\partial \alpha_1}=\frac{\partial v_0^*}{\partial \alpha_1} \text{ or } N^h_{121}=0,$$

$$\text{either } \phi_1 = \phi_1^* \text{ or } D^g_1-\frac{\partial B^g_{11}}{\partial \alpha_1}-2\frac{\partial B^g_{12}}{\partial \alpha_2}+2B^{g'}_{13}=0, \quad \text{either } \frac{\partial \phi_1}{\partial \alpha_1}=\frac{\partial \phi_1^*}{\partial \alpha_1} \text{ or } B^g_{11}=0,$$

$$\text{either } \phi_0 = \phi_0^* \text{ or } D^a_1-\frac{\partial B^a_{11}}{\partial \alpha_1}-2\frac{\partial B^a_{12}}{\partial \alpha_2}+2B^{a'}_{13}=0, \quad \text{either } \frac{\partial \phi_0}{\partial \alpha_1}=\frac{\partial \phi_0^*}{\partial \alpha_1} \text{ or } B^a_{11}=0, \tag{67}$$

On edges $\alpha_2 = 0$ and $\alpha_2 = b$

$$\text{either } v_0 = v_0^* \text{ or } N_{22}-\frac{\partial N^h_{222}}{\partial \alpha_2}-\frac{\partial N^h_{221}}{\partial \alpha_1}-\frac{\partial N^h_{122}}{\partial \alpha_1}=0, \quad \text{either } \frac{\partial v_0}{\partial \alpha_2}=\frac{\partial v_0^*}{\partial \alpha_2} \text{ or } N^h_{222}=0,$$

$$\text{either } w_0 = w_0^* \text{ or } \frac{\partial M_{22}}{\partial \alpha_2}+2\frac{\partial M_{12}}{\partial \alpha_1}-\frac{\partial^2 M^h_{222}}{\partial \alpha_2^2}-\frac{\partial^2 M^h_{221}}{\partial \alpha_2 \partial \alpha_1}+\frac{\partial N^h_{223}}{\partial \alpha_2}-2\frac{\partial^2 M^h_{122}}{\partial \alpha_1 \partial \alpha_2}+2\frac{\partial N^h_{123}}{\partial \alpha_1}=0,$$

$$\text{either } \frac{\partial w_0}{\partial \alpha_2}=\frac{\partial w_0^*}{\partial \alpha_2} \text{ or } -M_{22}+\frac{\partial M^h_{222}}{\partial \alpha_2}+\frac{\partial M^h_{221}}{\partial \alpha_1}-N^h_{223}+2\frac{\partial M^h_{122}}{\partial \alpha_1}=0,$$

$$\text{either } \frac{\partial w_0}{\partial \alpha_1}=\frac{\partial w_0^*}{\partial \alpha_1} \text{ or } \frac{\partial M^h_{112}}{\partial \alpha_1}+2\frac{\partial M^h_{121}}{\partial \alpha_1}=0, \quad \text{either } \frac{\partial^2 w_0}{\partial \alpha_2^2}=\frac{\partial^2 w_0^*}{\partial \alpha_2^2} \text{ or } M^h_{222}=0,$$

$$\text{either } u_0 = u_0^* \text{ or } N_{12}-\frac{\partial N^h_{112}}{\partial \alpha_1}-\frac{\partial N^h_{122}}{\partial \alpha_2}-\frac{\partial N^h_{121}}{\partial \alpha_1}=0, \quad \text{either } \frac{\partial u_0}{\partial \alpha_2}=\frac{\partial u_0^*}{\partial \alpha_2} \text{ or } N^h_{122}=0,$$

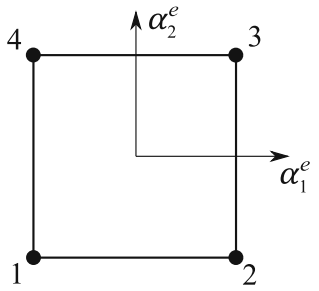

Fig. 2 A two-dimensional four-noded rectangular element. Here α_1^e and α_2^e denote the corresponding local coordinates

$$\text{either } \phi_1 = \phi_1^* \text{ or } D_2^g - \frac{\partial B_{22}^g}{\partial \alpha_2} - 2\frac{\partial B_{12}^g}{\partial \alpha_1} + 2B_{23}^{g'} = 0, \quad \text{either } \frac{\partial \phi_1}{\partial \alpha_2} = \frac{\partial \phi_1^*}{\partial \alpha_2} \text{ or } B_{22}^g = 0,$$
$$\text{either } \phi_0 = \phi_0^* \text{ or } D_2^a - \frac{\partial B_{22}^a}{\partial \alpha_2} - 2\frac{\partial B_{12}^a}{\partial \alpha_1} + 2B_{23}^{a'} = 0, \quad \text{either } \frac{\partial \phi_0}{\partial \alpha_2} = \frac{\partial \phi_0^*}{\partial \alpha_2} \text{ or } B_{22}^a = 0. \tag{68}$$

The boundary conditions on the corners of the flexoelectric plate are obtained as:

$$\begin{aligned}
&\text{either } w_0 = w_0^* \text{ or } 2M_{12} + 2N_{123}^h = 0, \text{ either } \frac{\partial w_0}{\partial \alpha_1} = \frac{\partial w_0^*}{\partial \alpha_1} \text{ or } M_{112}^h + 2M_{121}^h = 0,\\
&\text{either } \frac{\partial w_0}{\partial \alpha_2} = \frac{\partial w_0^*}{\partial \alpha_2} \text{ or } M_{221}^h + 2M_{122}^h = 0, \text{ either } u_0 = u_0^* \text{ or } N_{112}^h + N_{121}^h = 0,\\
&\text{either } v_0 = v_0^* \text{ or } N_{221}^h + N_{122}^h = 0,\\
&\text{either } \phi_1 = \phi_1^* \text{ or } B_{12}^g = 0,\\
&\text{either } \phi_0 = \phi_0^* \text{ or } B_{12}^a = 0.
\end{aligned} \tag{69}$$

3 Finite element formulation

This section presents the development of coupled finite element framework for a flexoelectric plate deforming under combined electrical and mechanical loads. Electromechanically coupled C^2 continuous conforming and non-conforming finite elements are developed to analyze actuator and sensor response of the flexoelectric composite plates.

3.1 2D shape functions

A two-dimensional four-noded rectangular element (shown in Fig. 2) is used to discretize the plate. The essential boundary conditions presented in Eqs. (67)–(69) involve second-order derivatives of w_0 with respect to α_1 and α_2. Thus, the shape functions for w_0 need to satisfy C^2 continuity. Similarly, the continuity requirement for shape functions of u_0, v_0, ϕ_1 and ϕ_0 is C^1, as essential boundary conditions consisting of these variables have first-order derivative terms. The development of C^1 and C^2 continuous shape functions for a four-noded rectangular element is discussed below.

C^1 Continuous shape functions: The field variables u_0, v_0, ϕ_1 and ϕ_0 are interpolated using C^1 continuous shape functions within each element. As discussed earlier, these field variables and their first-order derivatives are considered as the primary variables at each node. For instance, the shape functions are developed for in-plane displacement u_0. As per standard finite element procedure, u_0, $\frac{\partial u_0}{\partial \alpha_1}$ and $\frac{\partial u_0}{\partial \alpha_2}$ are nodal degrees of freedom and should be continuous across the element boundaries. For the standard conforming element, along with u_0, $\frac{\partial u_0}{\partial \alpha_1}$ and $\frac{\partial u_0}{\partial \alpha_2}$, an additional nodal degree of freedom $\frac{\partial^2 u_0}{\partial \alpha_1 \partial \alpha_2}$ is considered, to enforce the continuity

of $\frac{\partial u_0}{\partial \alpha_1}$ and $\frac{\partial u_0}{\partial \alpha_2}$ across the element boundaries [60]. For a four-noded element with four degrees of freedom per node, a sixteen-term polynomial function of α_1^e and α_2^e is used for the approximation of u_0 as follows:

$$\begin{aligned} u_0 &= c_1^u + c_2^u\alpha_1^e + c_3^u\alpha_2^e + c_4^u(\alpha_1^e)^2 + c_5^u\alpha_1^e\alpha_2^e + c_6^u(\alpha_2^e)^2 + c_7^u(\alpha_1^e)^3 + c_8^u(\alpha_1^e)^2\alpha_2^e \\ &\quad + c_9^u\alpha_1^e(\alpha_2^e)^2 + c_{10}^u(\alpha_2^e)^3 + c_{11}^u(\alpha_1^e)^3\alpha_2^e + c_{11}^u(\alpha_1^e)^2(\alpha_2^e)^2 + c_{13}^u\alpha_1^e(\alpha_2^e)^3 \\ &\quad + c_{14}^u(\alpha_1^e)^3(\alpha_2^e)^2 + c_{15}^u(\alpha_1^e)^2(\alpha_2^e)^3 + c_{16}^u(\alpha_1^e)^3(\alpha_2^e)^3 \\ &= [N_1^c\ N_2^c\ N_3^c ... N_{16}^c][\tilde{\mathbf{u}}^{\mathbf{c}[1]}\ \tilde{\mathbf{u}}^{\mathbf{c}[2]}\ \tilde{\mathbf{u}}^{\mathbf{c}[3]}\ \tilde{\mathbf{u}}^{\mathbf{c}[4]}]^{\mathrm{T}} = \mathbf{N}^{\mathbf{c}}\hat{\mathbf{u}}^{\mathbf{c}}, \end{aligned} \tag{70}$$

where c_j^u $(j = 1, 2, 3...16)$ are interpolation constants for conforming element, α_1^e and α_2^e are two-dimensional elemental coordinates shown in Fig. 2, $[N_1^c\ N_2^c\ N_3^c ... N_{16}^c]$ are C^1 continuous shape functions for a four-noded conforming element and $\tilde{\mathbf{u}}^{\mathbf{c}[i]} = [u_0^{[i]}\ u_{0,1}^{[i]}\ u_{0,2}^{[i]}\ u_{0,12}^{[i]}]$. Here, superscript $[i]$ represents the node number, and the subscripts $(\cdot)_{,1}$ and $(\cdot)_{,2}$ denote the differentiation of the quantity with respect to α_1 and α_2, respectively. Similarly, $(\cdot)_{,12}$ denotes the second-order differentiation of the quantity with respect to both α_1 and α_2. The conforming element allows the continuity of considered degrees of freedom along all four edges of the element, and it also shows a monotonic convergence of the finite element results.

Alternatively, a non-conforming element with three degrees of freedom at each node can be used, i.e., $\left(u_0, \frac{\partial u_0}{\partial \alpha_1}, \frac{\partial u_0}{\partial \alpha_2}\right)$. In this case, a twelve-term polynomial function of α_1 and α_2 is required for the approximation of u_0 as follows:

$$\begin{aligned} u_0 &= n_1^u + n_2^u\alpha_1^e + n_3^u\alpha_2^e + n_4^u(\alpha_1^e)^2 + n_5^u\alpha_1^e\alpha_2^e + n_6^u(\alpha_2^e)^2 + n_7^u(\alpha_1^e)^3 + n_8^u(\alpha_1^e)^2\alpha_2^e \\ &\quad + n_9^u\alpha_1^e(\alpha_2^e)^2 + n_{10}^u(\alpha_2^e)^3 + n_{11}^u(\alpha_1^e)^3\alpha_2^e + n_{12}^u\alpha_1^e(\alpha_2^e)^3 \\ &= [N_1\ N_2\ N_3 ... N_{12}][\tilde{\mathbf{u}}^{[1]}\ \tilde{\mathbf{u}}^{[2]}\ \tilde{\mathbf{u}}^{[3]}\ \tilde{\mathbf{u}}^{[4]}]^{\mathrm{T}} = \mathbf{N}\hat{\mathbf{u}}, \end{aligned} \tag{71}$$

where n_j^u $(j = 1, 2, 3...12)$ denote interpolation constants for a non-conforming element and $[N_1\ N_2\ N_3 ... N_{12}]$ are C^1 continuous shape functions for the non-conforming element. Here, nodal degree of freedom has three degrees of freedom, i.e., $\tilde{\mathbf{u}}^{[i]} = [u_0^{[i]}\ u_{0,1}^{[i]}\ u_{0,2}^{[i]}]$. The non-conforming element satisfies the continuity of u_0 and $\frac{\partial u_0}{\partial \alpha_1}$ along the edges of the element parallel to α_1^e and u_0 and $\frac{\partial u_0}{\partial \alpha_2}$ along the edges of the element parallel to α_2^e. The field variables v_0, ϕ_1 and ϕ_0 are also expressed in terms of C^1 continuous shape functions and elemental degrees of freedom as follows:

$$v_0 = [N_1\ N_2\ N_3 ... N_{12}][\tilde{\mathbf{v}}^{[1]}\ \mathbf{v}^{[2]}\ \mathbf{v}^{[3]}\ \tilde{\mathbf{v}}^{[4]}]^{\mathrm{T}} = \mathbf{N}\hat{\mathbf{v}}, \tag{72}$$

$$\phi_1 = [N_1\ N_2\ N_3 ... N_{12}][\tilde{\boldsymbol{\phi}}_1^{[1]}\ \tilde{\boldsymbol{\phi}}_1^{[2]}\ \tilde{\boldsymbol{\phi}}_1^{[3]}\ \tilde{\boldsymbol{\phi}}_1^{[4]}]^{\mathrm{T}} = \mathbf{N}\hat{\boldsymbol{\phi}}_1, \tag{73}$$

$$\phi_0 = [N_1\ N_2\ N_3 ... N_{12}][\tilde{\boldsymbol{\phi}}_a^{[1]}\ \tilde{\boldsymbol{\phi}}_a^{[2]}\ \tilde{\boldsymbol{\phi}}_a^{[3]}\ \tilde{\boldsymbol{\phi}}_a^{[4]}]^{\mathrm{T}} = \mathbf{N}\hat{\boldsymbol{\phi}}_a, \tag{74}$$

where $\tilde{\mathbf{v}}^{[i]} = [v_0^{[i]}\ v_{0,1}^{[i]}\ v_{0,2}^{[i]}]$, $\tilde{\boldsymbol{\phi}}_1^{[i]} = [\phi_1^{[i]}\ \phi_{1,1}^{[i]}\ \phi_{1,2}^{[i]}]$ and $\tilde{\boldsymbol{\phi}}_a^{[i]} = [\phi_0^{[i]}\ \phi_{a,1}^{[i]}\ \phi_{a,2}^{[i]}]$.

C^2 Continuous shape functions: The shape functions of the transverse displacement w_0 have C^2 continuity requirement within the element. The essential boundary conditions (67)–(69) have w_0, $\frac{\partial w_0}{\partial \alpha_1}$, $\frac{\partial w_0}{\partial \alpha_2}$, $\frac{\partial^2 w_0}{\partial \alpha_1^2}$ and $\frac{\partial^2 w_0}{\partial \alpha_2^2}$ as primary variables. The primary variables are considered as nodal degrees of freedom and additional nodal degrees of freedom $\frac{\partial^2 w_0}{\partial \alpha_1 \partial \alpha_2}$, $\frac{\partial^3 w_0}{\partial \alpha_1^2 \partial \alpha_2}$, $\frac{\partial^3 w_0}{\partial \alpha_1 \partial \alpha_2^2}$ and $\frac{\partial^4 w_0}{\partial \alpha_1^2 \partial \alpha_2^2}$ are needed to considered at each node to ensure the continuity across the element boundaries as in case of conforming element developed by Babu and Patel [61]. A thirty-six-term polynomial function is used to approximate w_0, which is given by:

$$\begin{aligned} w_0 &= c_1^w + c_2^w\alpha_1^e + c_3^w\alpha_2^e + c_4^w(\alpha_1^e)^2 + c_5^w\alpha_1^e\alpha_2^e + c_6^w(\alpha_2^e)^2 + c_7^w(\alpha_1^e)^3 + c_8^w(\alpha_1^e)^2\alpha_2^e \\ &\quad + c_9^w\alpha_1^e(\alpha_2^e)^2 + c_{10}^w(\alpha_2^e)^3 + c_{11}^w(\alpha_1^e)^4 + c_{12}^w(\alpha_1^e)^3\alpha_2^e + c_{13}^w(\alpha_1^e)^2(\alpha_2^e)^2 \end{aligned}$$

$$
\begin{aligned}
&+ c_{14}^{w}\alpha_1^e(\alpha_2^e)^3 + c_{15}^{w}(\alpha_2^e)^4 + c_{16}^{w}(\alpha_1^e)^5 + c_{17}^{w}(\alpha_1^e)^4\alpha_2^e + c_{18}^{w}(\alpha_1^e)^3(\alpha_2^e)^2 \\
&+ c_{19}^{w}(\alpha_1^e)^2(\alpha_2^e)^3 + c_{20}^{w}\alpha_1^e(\alpha_2^e)^4 + c_{21}^{w}(\alpha_2^e)^5 + c_{22}^{w}\alpha_2^e(\alpha_1^e)^5 + c_{23}^{w}(\alpha_1^e)^4(\alpha_2^e)^2 \\
&+ c_{24}^{w}(\alpha_1^e)^3(\alpha_2^e)^3 + c_{25}^{w}(\alpha_1^e)^2(\alpha_2^e)^4 + c_{26}^{w}\alpha_1^e(\alpha_2^e)^5 + c_{27}^{w}(\alpha_1^e)^5(\alpha_2^e)^2 \\
&+ c_{28}^{w}(\alpha_1^e)^4(\alpha_2^e)^3 + c_{29}^{w}(\alpha_1^e)^3(\alpha_2^e)^4 + c_{30}^{w}(\alpha_1^e)^2(\alpha_2^e)^5 + c_{31}^{w}(\alpha_1^e)^5(\alpha_2^e)^3 \\
&+ c_{32}^{w}(\alpha_1^e)^4(\alpha_2^e)^4 + c_{33}^{w}(\alpha_1^e)^3(\alpha_2^e)^5 + c_{34}^{w}(\alpha_1^e)^5(\alpha_2^e)^4 + c_{35}^{w}(\alpha_1^e)^4(\alpha_2^e)^5 + c_{36}^{w}(\alpha_1^e)^5(\alpha_2^e)^5 \\
&= [P_1^c \;\; P_2^c \;\; P_3^c ... P_{36}^c][\tilde{\mathbf{w}}^{\mathbf{c}[1]} \;\; \tilde{\mathbf{w}}^{\mathbf{c}[2]} \;\; \tilde{\mathbf{w}}^{\mathbf{c}[3]} \;\; \tilde{\mathbf{w}}^{\mathbf{c}[4]}]^{\mathrm{T}} = \mathbf{P}^{\mathbf{c}}\hat{\mathbf{w}}^{\mathbf{c}},
\end{aligned} \tag{75}
$$

where c_j^w $(j = 1, 2, 3...36)$ are interpolation constants for the conforming element, $[P_1^c \;\; P_2^c ... P_{36}^c]$ are C^2 continuous shape functions for w_0 and $\tilde{\mathbf{w}}^{\mathbf{c}[i]} = [w_0^{[i]} \;\; w_{0,1}^{[i]} \;\; w_{0,2}^{[i]} \;\; w_{0,12}^{[i]} \;\; w_{0,11}^{[i]} \;\; w_{0,22}^{[i]} \;\; w_{0,112}^{[i]} \;\; w_{0,221}^{[i]} \;\; w_{0,1122}^{[i]}]$.

On the other hand, for the non-conforming element, only six degrees of freedom corresponding to transverse displacement $\left(w_0, \frac{\partial w_0}{\partial \alpha_1}, \frac{\partial w_0}{\partial \alpha_2}, \frac{\partial^2 w_0}{\partial \alpha_1^2}, \frac{\partial^2 w_0}{\partial \alpha_1 \partial \alpha_2}, \frac{\partial^2 w_0}{\partial \alpha_2^2}\right)$ are considered at each node. While continuity of all the derivatives is not imposed on all edges of an element, the non-conforming element gives fairly accurate results while providing greater computational efficiency compared to the conforming element. A twenty-four-term polynomial function is used to approximate w_0, given as follows:

$$
\begin{aligned}
w_0 =& n_1^w + n_2^w\alpha_1^e + n_3^w\alpha_2^e + n_4^w(\alpha_1^e)^2 + n_5^w\alpha_1^e\alpha_2^e + n_6^w(\alpha_2^e)^2 + n_7^w(\alpha_1^e)^3 + n_8^w(\alpha_1^e)^2\alpha_2^e \\
&+ n_9^w\alpha_1^e(\alpha_2^e)^2 + n_{10}^w(\alpha_2^e)^3 + n_{11}^w(\alpha_1^e)^4 + n_{12}^w(\alpha_1^e)^3\alpha_2^e + n_{13}^w(\alpha_1^e)^2(\alpha_2^e)^2 \\
&+ n_{14}^w\alpha_1^e(\alpha_2^e)^3 + n_{15}^w(\alpha_2^e)^4 + n_{16}^w(\alpha_1^e)^5 + n_{17}^w(\alpha_1^e)^4\alpha_2^e + n_{18}^w(\alpha_1^e)^3(\alpha_2^e)^2 \\
&+ n_{19}^w(\alpha_1^e)^2(\alpha_2^e)^3 + n_{20}^w\alpha_1^e(\alpha_2^e)^4 + n_{21}^w(\alpha_2^e)^5 + n_{22}^w\alpha_2^e(\alpha_1^e)^5 + n_{23}^w(\alpha_1^e)^3(\alpha_2^e)^3 + n_{24}^w\alpha_1^e(\alpha_2^e)^5 \\
=& [P_1 \;\; P_2 \;\; P_3 ... P_{24}][\tilde{\mathbf{w}}^{[1]} \;\; \tilde{\mathbf{w}}^{[2]} \;\; \tilde{\mathbf{w}}^{[3]} \;\; \tilde{\mathbf{w}}^{[4]}]^{\mathrm{T}} = \mathbf{P}\hat{\mathbf{w}},
\end{aligned} \tag{76}
$$

where n_j^w $(j = 1, 2, 3...24)$ are interpolation constants for a non-conforming element, $[P_1 \;\; P_2 \;\; P_3 ... P_{24}]$ are C^2 continuous shape functions. In case of non-conforming element, $\tilde{\mathbf{w}}^{[i]} = [w_0^{[i]} \;\; w_{0,1}^{[i]} \;\; w_{0,2}^{[i]} \;\; w_{0,12}^{[i]} \;\; w_{0,11}^{[i]} \;\; w_{0,22}^{[i]}]$. It allows the continuity of w_0, $\frac{\partial w_0}{\partial \alpha_1}$, $\frac{\partial w_0}{\partial \alpha_2}$, $\frac{\partial^2 w_0}{\partial \alpha_1 \partial \alpha_2}$ and $\frac{\partial^2 w_0}{\partial \alpha_1^2}$ along the edges of the element parallel to α_1^e and w_0, $\frac{\partial w_0}{\partial \alpha_1}$, $\frac{\partial w_0}{\partial \alpha_2}$, $\frac{\partial^2 w_0}{\partial \alpha_1 \partial \alpha_2}$ and $\frac{\partial^2 w_0}{\partial \alpha_2^2}$ along the edges of the element parallel to α_2^e.

It may be noted that for a classical plate bending element (ignoring strain gradient effects), the conforming element has only one extra nodal degree of freedom than non-conforming element [60], as the transverse displacement w_0 is C^1 continuous. The extra nodal degree of freedom, i.e., $\frac{\partial^2 w_0}{\partial \alpha_1 \partial \alpha_2}$ for conforming element does not affect the computational efficiency of conforming element significantly in comparison with the non-conforming element.

However, due to electromechanical gradient effects considered in the present flexoelectric pate theory, the non-conforming element is computationally more efficient than the conforming element significantly. The non-conforming element has a total of 18 degrees of freedom per node and total of 72 degrees of freedom per element, while the conforming element has total of 25 degrees of freedom per node and total of 100 degrees of freedom per element. Due to lesser number of degrees of freedom, the non-conforming element is computationally more efficient than the conforming element.

3.2 Matrix representation

The components of strain tensor $\overline{\mathbf{S}}$ are represented in a matrix form as:

$$
\overline{\mathbf{S}}_{\{3\times 1\}} = \mathbf{H}^{\mathbf{S}}{}_{\{3\times 6\}}\mathbf{L}^{\mathbf{S}}{}_{\{6\times 5\}}\mathbf{d}_{\{5\times 1\}}, \tag{77}
$$

where the matrices $\mathbf{H^S}$, $\mathbf{L^S}$ and $\mathbf{d}$ are given by

$$\mathbf{H^S} = \begin{bmatrix} 1 & -\alpha_3 & 0 & 0 & 0 & 0 \\ 0 & 0 & 1 & -\alpha_3 & 0 & 0 \\ 0 & 0 & 0 & 0 & \frac{1}{2} & -\alpha_3 \end{bmatrix}, \quad \mathbf{L^S} = \begin{bmatrix} \frac{\partial}{\partial\alpha_1} & 0 & 0 & 0 & 0 \\ 0 & 0 & \frac{\partial^2}{\partial\alpha_1^2} & 0 & 0 \\ 0 & \frac{\partial}{\partial\alpha_2} & 0 & 0 & 0 \\ 0 & 0 & \frac{\partial^2}{\partial\alpha_2^2} & 0 & 0 \\ \frac{\partial}{\partial\alpha_2} & \frac{\partial}{\partial\alpha_1} & 0 & 0 & 0 \\ 0 & 0 & \frac{\partial^2}{\partial\alpha_1\partial\alpha_2} & 0 & 0 \end{bmatrix}, \tag{78}$$

$$\mathbf{d} = [u_0 \ v_0 \ w_0 \ \phi_1 \ \phi_0]\,. \tag{79}$$

Similarly, the strain gradient components $\overline{\mathbf{G}}$, electric field components $\overline{\mathbf{E}}$ and electric field gradient components $\overline{\mathbf{K}}$ are also represented in a matrix form as follows:

$$\overline{\mathbf{G}}_{\{9\times1\}} = \mathbf{H^G}_{\{9\times13\}}\mathbf{L^G}_{\{13\times5\}}\mathbf{d}_{\{5\times1\}}, \tag{80}$$

$$\overline{\mathbf{E}}_{\{3\times1\}} = \mathbf{H^E}_{\{3\times6\}}\mathbf{L^E}_{\{6\times5\}}\mathbf{d}_{\{5\times1\}}, \tag{81}$$

$$\overline{\mathbf{K}}_{\{6\times1\}} = \mathbf{H^K}_{\{6\times12\}}\mathbf{L^K}_{\{12\times5\}}\mathbf{d}_{\{5\times1\}}. \tag{82}$$

The matrices $\mathbf{H^G}$, $\mathbf{H^E}$ and $\mathbf{H^K}$; and operator matrices $\mathbf{L^G}$, $\mathbf{L^E}$ and $\mathbf{L^K}$ can be obtained following the procedure described in (77)–(79).

In what follows, the elemental expressions for strain components $\overline{\mathbf{S}}$, strain gradient components $\overline{\mathbf{G}}$, electric field components $\overline{\mathbf{E}}$ and electric field gradient components $\overline{\mathbf{K}}$ are obtained for each element by expressing the field variables $(u_0, v_0, w_0, \phi_1, \phi_0)$ in terms of the shape functions and nodal degrees of freedom as follows:

$$\begin{aligned} \overline{\mathbf{S}}^{(l)} &= \mathbf{H^S}\mathbf{B^S}^{(l)}\hat{\mathbf{d}}^{(l)}, \quad \overline{\mathbf{G}}^{(l)} = \mathbf{H^G}\mathbf{B^G}^{(l)}\hat{\mathbf{d}}^{(l)}, \\ \overline{\mathbf{E}}^{(l)} &= \mathbf{H^E}\mathbf{B^E}^{(l)}\hat{\mathbf{d}}^{(l)}, \quad \overline{\mathbf{K}}^{(l)} = \mathbf{H^K}\mathbf{B^K}^{(l)}\hat{\mathbf{d}}^{(l)}, \end{aligned} \tag{83}$$

where $(\cdot)^{(l)}$ denotes the elemental quantities for the l^{th} element; the matrices $\mathbf{B^S}^{(l)}$, $\mathbf{B^G}^{(l)}$, $\mathbf{B^E}^{(l)}$ and $\mathbf{B^K}^{(l)}$ are obtained from the operator matrices $\mathbf{L^S}$, $\mathbf{L^G}$, $\mathbf{L^E}$ and $\mathbf{L^K}$ acting on the respective shape functions at every node of the element; and $\hat{\mathbf{d}} = [\tilde{\mathbf{d}}^{[1]}\ \tilde{\mathbf{d}}^{[2]}\ \tilde{\mathbf{d}}^{[3]}\ \tilde{\mathbf{d}}^{[4]}]^{\mathrm{T}}$ is a vector consisting of mechanical and electrical degrees of freedom for l^{th} element where

$$\tilde{\mathbf{d}}^{[i]} = [\tilde{\mathbf{u}}^{[i]}\ \tilde{\mathbf{v}}^{[i]}\ \tilde{\mathbf{w}}^{[i]}\ \tilde{\boldsymbol{\phi}_1}^{[i]}\ \tilde{\boldsymbol{\phi}_0}^{[i]}].$$

3.3 Derivation of finite element formulation

In what follows, the finite element formulation is derived using the potential energy minimization principle (4). The variation of free energy $\Omega^{(l)}$ for an element is obtained by using the elemental strain, strain gradient, electric field and electric field gradient components from Eqs. (77)–(82), and integrating across the element thickness similar to Eq. (57) as follows:

$$\begin{aligned} \int_{\mathcal{V}_0^{(l)}} \delta\Omega^{(l)}\mathrm{d}V &= \int_{\mathcal{A}_0^{(l)}} \int_{\alpha_3=\frac{-h}{2}}^{\alpha_3=\frac{h}{2}} \delta\Omega^{(l)}\,\mathrm{d}\alpha_3\mathrm{d}\alpha_2^e\mathrm{d}\alpha_1^e \\ &= \int_{\mathcal{A}_0^{(l)}} [(\delta\hat{\mathbf{d}}^{(l)})^{\mathrm{T}}(\mathbf{B^S}^{(l)})^{\mathrm{T}}\mathbf{D^{SS}}\mathbf{B^S}^{(l)}\hat{\mathbf{d}}^{(l)} - (\delta\hat{\mathbf{d}}^{(l)})^{\mathrm{T}}(\mathbf{B^S}^{(l)})^{\mathrm{T}}\mathbf{D^{SK}}\mathbf{B^K}^{(l)}\hat{\mathbf{d}}^{(l)} \\ &\quad + (\delta\hat{\mathbf{d}}^{(l)})^{\mathrm{T}}(\mathbf{B^G}^{(l)})^{\mathrm{T}}\mathbf{D^{GG}}\mathbf{B^G}^{(l)}\hat{\mathbf{d}}^{(l)} - (\delta\hat{\mathbf{d}}^{(l)})^{\mathrm{T}}(\mathbf{B^G}^{(l)})^{\mathrm{T}}\mathbf{D^{GE}}\mathbf{B^E}^{(l)}\hat{\mathbf{d}}^{(l)} \\ &\quad - (\delta\hat{\mathbf{d}}^{(l)})^{\mathrm{T}}(\mathbf{B^E}^{(l)})^{\mathrm{T}}\mathbf{D^{EE}}\mathbf{B^E}^{(l)}\hat{\mathbf{d}}^{(l)} - (\delta\hat{\mathbf{d}}^{(l)})^{\mathrm{T}}(\mathbf{B^E}^{(l)})^{\mathrm{T}}\mathbf{D^{EG}}\mathbf{B^G}^{(l)}\hat{\mathbf{d}}^{(l)} \\ &\quad - (\delta\hat{\mathbf{d}}^{(l)})^{\mathrm{T}}(\mathbf{B^K}^{(l)})^{\mathrm{T}}\mathbf{D^{KK}}\mathbf{B^K}^{(l)}\hat{\mathbf{d}}^{(l)} - (\delta\hat{\mathbf{d}}^{(l)})^{\mathrm{T}}(\mathbf{B^K}^{(l)})^{\mathrm{T}}\mathbf{D^{KS}}\mathbf{B^S}^{(l)}\hat{\mathbf{d}}^{(l)}]\mathrm{d}\alpha_1^e\alpha_2^e. \end{aligned} \tag{84}$$

Here, $\mathcal{A}_0^{(l)}$ represents the surface area of the l^{th} element. The matrices $\mathbf{D^{SS}}$, $\mathbf{D^{SK}}$, $\mathbf{D^{GG}}$, $\mathbf{D^{GE}}$, $\mathbf{D^{EE}}$, $\mathbf{D^{EG}}$, $\mathbf{D^{KK}}$ and $\mathbf{D^{KS}}$ are defined in Appendix B. The two-dimensional integration in (84) is performed using the Gauss Quadrature method and expressed in terms of elemental stiffness matrices as follows:

$$\int_{\mathcal{V}_0^{(l)}} \delta\Omega^{(l)} \mathrm{d}V = (\delta\hat{\mathbf{d}}^{(l)})^{\mathrm{T}}[\mathbf{K^{SS}}^{(l)} - \mathbf{K^{SK}}^{(l)} + \mathbf{K^{GG}}^{(l)} - \mathbf{K^{GE}}^{(l)} - \mathbf{K^{EE}}^{(l)} - \mathbf{K^{EG}}^{(l)} - \mathbf{K^{KK}}^{(l)} - \mathbf{K^{KS}}]\hat{\mathbf{d}}^{(l)}, \tag{85}$$

The expression of matrices $\mathbf{K^{SS}}$, $\mathbf{K^{SK}}$, $\mathbf{K^{GG}}$, $\mathbf{K^{GE}}$, $\mathbf{K^{EE}}$, $\mathbf{K^{EG}}$, $\mathbf{K^{KK}}$ and $\mathbf{K^{KS}}$ are defined in Appendix B. Finally, the variation in the total free energy $\delta\Omega$ for the plate is obtained by assembling the elemental energies and summing over all the elements to obtain the global stiffness matrix given by:

$$\begin{aligned}\int_{\mathcal{V}_0} \delta\Omega \mathrm{d}V &= \sum_{l=1}^{n_e} \{(\delta\hat{\mathbf{d}}^{(l)})^{\mathrm{T}}[\mathbf{K^{SS}}^{(l)} - \mathbf{K^{SK}}^{(l)} + \mathbf{K^{GG}}^{(l)} - \mathbf{K^{GE}}^{(l)} - \mathbf{K^{EE}}^{(l)} - \mathbf{K^{EG}}^{(l)} - \mathbf{K^{KK}}^{(l)} - \mathbf{K^{KS}}]\hat{\mathbf{d}}^{(l)}\} \\ &= \delta\overline{\mathbf{d}}^{\mathrm{T}}\overline{\mathbf{K}}_{\mathbf{g}}\,\overline{\mathbf{d}},\end{aligned} \tag{86}$$

where $\overline{\mathbf{K}}_{\mathbf{g}}$ is the global stiffness matrix, $\overline{\mathbf{d}}$ denotes the global field variable vector consisting of the combined degrees of freedom of all the nodes, and n_e is the total number of elements used for discretization of the flexoelectric plate. The variation of the work done due to external loads on each element is expressed in terms of the elemental force vector as

$$\delta\omega^{(l)} = \int_{\alpha_1^e}\int_{\alpha_2^e} [q_3^{(l)}\delta w_0^{(l)} + \rho_s^{(l)}\delta\phi_0^{(l)}]\mathrm{d}\alpha_2^e\mathrm{d}\alpha_1^e = (\delta\hat{\mathbf{d}}^{(l)})^{\mathrm{T}}\mathbf{F_{ge}}^{(l)}, \tag{87}$$

where $\mathbf{F_{ge}}$ denotes the elemental force vector. Again, performing assembly over all the elements, the variation in the total external work done is evaluated in terms of the global force vector as

$$\delta\omega = \sum_{l=1}^{n_e} (\delta\mathbf{d}^{(l)})^{\mathrm{T}}\mathbf{F_{ge}}^{(l)} = \delta\overline{\mathbf{d}}^{\mathrm{T}}\overline{\mathbf{F}}_{\mathbf{g}}, \tag{88}$$

where $\overline{\mathbf{F}}_{\mathbf{g}}$ represents the global force vector, which includes both mechanical and electrical load terms. Finally, using the potential energy minimization principle, the finite element governing equations, in matrix form, are obtained as

$$\int_{\mathcal{V}_0} \delta\Omega \mathrm{d}V - \delta\omega = 0 \quad \Longrightarrow \quad \overline{\mathbf{K}}_{\mathbf{g}}\,\overline{\mathbf{d}} = \overline{\mathbf{F}}_{\mathbf{g}}. \tag{89}$$

These global finite element equations are solved algebraically to obtain nodal values of mechanical displacements and electrostatic potential. The formulation is used to analyze the flexoelectric plate in both sensor and actuator modes. The plate equations are also solved analytically for simply supported boundary conditions using Navier's method, and the results are utilized to verify the accuracy of our finite element results. The details of analytical solution are given in Appendix C.

4 Results and discussion

Finite element framework discussed in Sect. 3 is implemented to analyze the sensor and actuator response of flexoelectric composite plates. A number of examples are considered in the subsequent sections and parametric studies are performed to analyze the effect of boundary conditions, loading conditions, length scale parameters, thickness of the flexoelectric layer, etc. A MATLAB program is written to compute the global stiffness matrix and force vector. The clamped, free or simply supported boundary conditions are applied on all four edges. The boundary conditions are abbreviated as follows:

1. SSSS: Simply supported on all four edges.
2. SCSS: Clamped on edge $\alpha_1 = a$, and simply supported on the remaining edges.
3. SSSC: Clamped on edge $\alpha_1 = 0$, and simply supported on the remaining edges.
4. SCSC: Clamped on edges $\alpha_1 = 0$ and $\alpha_1 = a$; simply supported on edges $\alpha_2 = 0$ and $\alpha_2 = b$.
5. FCFC: Clamped on edges $\alpha_1 = 0$ and $\alpha_1 = a$; free on edges $\alpha_2 = 0$ and $\alpha_2 = b$.

6. FFFC: Clamped on edge $\alpha_1 = 0$, and free on the remaining edges.

The equations corresponding to each boundary condition may be listed as follows:

Clamped (C):

On edges $\alpha_1 = 0$ and $\alpha_1 = a$

$$u_0 = N^h_{111} = w_0 = \frac{\partial w_0}{\partial \alpha_1} = \frac{\partial w_0}{\partial \alpha_2} = M^h_{111} = v_0 = N^h_{121} = 0,$$

On edges $\alpha_2 = 0$ and $\alpha_2 = b$

$$v_0 = N^h_{222} = w_0 = \frac{\partial w_0}{\partial \alpha_2} = \frac{\partial w_0}{\partial \alpha_1} = M^h_{222} = u_0 = N^h_{122} = 0,$$

Simply Supported (S):

On edges $\alpha_1 = 0$ and $\alpha_1 = a$

$$N_{11} - \frac{\partial N^h_{111}}{\partial \alpha_1} - \frac{\partial N^h_{112}}{\partial \alpha_2} - \frac{\partial N^h_{121}}{\partial \alpha_2} = \frac{\partial u_0}{\partial \alpha_1} = w_0 = 0,$$

$$- M_{11} + \frac{\partial M^h_{111}}{\partial \alpha_1} + \frac{\partial M^h_{112}}{\partial \alpha_2} - N^h_{113} + 2\frac{\partial M^h_{121}}{\partial \alpha_2} = 0,$$

$$\frac{\partial w_0}{\partial \alpha_2} = \frac{\partial^2 w_0}{\partial \alpha_1^2} = v_0 = N^h_{121} = 0,$$

On edges $\alpha_2 = 0$ and $\alpha_2 = b$

$$N_{22} - \frac{\partial N^h_{222}}{\partial \alpha_2} - \frac{\partial N^h_{221}}{\partial \alpha_1} - \frac{\partial N^h_{122}}{\partial \alpha_1} = \frac{\partial v_0}{\partial \alpha_2} = w_0 = 0,$$

$$- M_{22} + \frac{\partial M^h_{222}}{\partial \alpha_2} + \frac{\partial M^h_{221}}{\partial \alpha_1} - N^h_{223} + 2\frac{\partial M^h_{122}}{\partial \alpha_1} = 0,$$

$$\frac{\partial w_0}{\partial \alpha_1} = \frac{\partial^2 w_0}{\partial \alpha_2^2} = u_0 = N^h_{122} = 0,$$

Free (F):

On edges $\alpha_1 = 0$ and $\alpha_1 = a$

$$N_{11} - \frac{\partial N^h_{111}}{\partial \alpha_1} - \frac{\partial N^h_{112}}{\partial \alpha_2} - \frac{\partial N^h_{121}}{\partial \alpha_2} = N^h_{111} = 0,$$

$$\frac{\partial M_{11}}{\partial \alpha_1} + 2\frac{\partial M_{12}}{\partial \alpha_2} - \frac{\partial^2 M^h_{111}}{\partial \alpha_1^2} - \frac{\partial^2 M^h_{112}}{\partial \alpha_2 \partial \alpha_1} + \frac{\partial N^h_{113}}{\partial \alpha_1} - 2\frac{\partial^2 M^h_{121}}{\partial \alpha_1 \partial \alpha_2} + 2\frac{\partial N^h_{123}}{\partial \alpha_2} = 0,$$

$$- M_{11} + \frac{\partial M^h_{111}}{\partial \alpha_1} + \frac{\partial M^h_{112}}{\partial \alpha_2} - N^h_{113} + 2\frac{\partial M^h_{121}}{\partial \alpha_2} = \frac{\partial M^h_{221}}{\partial \alpha_2} + 2\frac{\partial M^h_{122}}{\partial \alpha_2} = 0,$$

$$M^h_{111} = N_{12} - \frac{\partial N^h_{221}}{\partial \alpha_2} - \frac{\partial N^h_{121}}{\partial \alpha_1} - \frac{\partial N^h_{122}}{\partial \alpha_2} = N^h_{121} = 0, \tag{90}$$

On edges $\alpha_2 = 0$ and $\alpha_2 = b$

$$N_{22} - \frac{\partial N^h_{222}}{\partial \alpha_2} - \frac{\partial N^h_{221}}{\partial \alpha_1} - \frac{\partial N^h_{122}}{\partial \alpha_1} = N^h_{222} = 0,$$

$$\frac{\partial M_{22}}{\partial \alpha_2} + 2\frac{\partial M_{12}}{\partial \alpha_1} - \frac{\partial^2 M^h_{222}}{\partial \alpha_2^2} - \frac{\partial^2 M^h_{221}}{\partial \alpha_2 \partial \alpha_1} + \frac{\partial N^h_{223}}{\partial \alpha_2} - 2\frac{\partial^2 M^h_{122}}{\partial \alpha_1 \partial \alpha_2} + 2\frac{\partial N^h_{123}}{\partial \alpha_1} = 0,$$

$$- M_{22} + \frac{\partial M^h_{222}}{\partial \alpha_2} + \frac{\partial M^h_{221}}{\partial \alpha_1} - N^h_{223} + 2\frac{\partial M^h_{122}}{\partial \alpha_1} = \frac{\partial M^h_{112}}{\partial \alpha_1} + 2\frac{\partial M^h_{121}}{\partial \alpha_1} = 0,$$

$$M^h_{222} = N_{12} - \frac{\partial N^h_{112}}{\partial \alpha_1} - \frac{\partial N^h_{122}}{\partial \alpha_2} - \frac{\partial N^h_{121}}{\partial \alpha_1} = N^h_{122} = 0. \tag{91}$$

The electrical boundary conditions are given by

Charge boundary conditions (CBC):

On edges $\alpha_1 = 0$ and $\alpha_1 = a$

$$D^g_1 - \frac{\partial B^g_{11}}{\partial \alpha_1} - 2\frac{\partial B^g_{12}}{\partial \alpha_2} + 2B^g_{13} = B^g_{11} = 0,$$

$$D^a_1 - \frac{\partial B^a_{11}}{\partial \alpha_1} - 2\frac{\partial B^a_{12}}{\partial \alpha_2} + 2B^a_{13} = B^a_{11} = 0,$$

On edges $\alpha_2 = 0$ and $\alpha_2 = b$

$$D^g_2 - \frac{\partial B^g_{22}}{\partial \alpha_2} - 2\frac{\partial B^g_{12}}{\partial \alpha_1} + 2B^g_{23} = B^g_{22} = 0,$$

$$D^a_2 - \frac{\partial B^a_{22}}{\partial \alpha_2} - 2\frac{\partial B^a_{12}}{\partial \alpha_1} + 2B^a_{23} =, B^a_{22} = 0. \tag{92}$$

Potential boundary conditions (PBC):

On edges $\alpha_1 = 0$ and $\alpha_1 = a$

$$\phi_1 = B^g_{11} = \phi_0 = B^a_{11} = 0,$$

On edges $\alpha_2 = 0$ and $\alpha_2 = b$

$$\phi_1 = B^g_{22} = \phi_0 = B^a_{22} = 0, \tag{93}$$

Higher-order potential boundary conditions (HPBC):

On edges $\alpha_1 = 0$ and $\alpha_1 = a$

$$\phi_1 = \frac{\partial \phi_1}{\partial \alpha_1} = \phi_0 = \frac{\partial \phi_0}{\partial \alpha_1} = 0,$$

On edges $\alpha_2 = 0$ and $\alpha_2 = b$

$$\phi_1 = \frac{\partial \phi_1}{\partial \alpha_2} = \phi_0 = \frac{\partial \phi_0}{\partial \alpha_2} = 0. \tag{94}$$

The finite element results are verified with the analytical solutions for simply supported boundary conditions. The contribution of converse flexoelectric effect in the overall response of a flexoelectric material-based sensor is studied and compared with the contribution of direct flexoelectric effect. The effective piezoelectric coefficient is calculated for the flexoelectric plate and compared with piezoelectric materials at different length scales. It is observed that both direct and converse flexoelectric effects are prominent at small scales, which makes flexoelectric materials suitable for applications in MEMS and NEMS.

4.1 Bending analysis of passive micro-plate

Our finite element results are verified for a passive simply supported isotropic micro-plate (of thickness in the micron range). The micro-plate is analyzed under a uniformly distributed load ($q = 1\ \mu\text{N}/\mu\text{m}^2$). The Young's modulus ($c$) and Poisson's ratio ($\upsilon$) of the plate are taken as: [42]

$$c = 1.44\ \text{GPa},\ \ \upsilon = 0.38. \tag{95}$$

Nondimensional maximum transverse deflection w/h is calculated using the modified strain gradient theory, i.e., $l_0 = l_1 = l_2$= 11.01 μm [42]. Convergence study is performed for both conforming and non-conforming finite elements, and the results are presented in Fig. 3 for different mesh sizes. Our finite element results converge for a mesh size of 12 × 12 and agree well with analytical results presented in Akgoz and Civalek [42]. For the mesh size of 12 × 12, the computational time taken by non-conforming element is 1.70 s, and conforming element takes 2.19 s.[1]

[1] All the simulations are performed using MATLAB 2019 on a Windows 10 pro desktop computed with 8 core processor having base frequency of 3.70 GHz and 48 GB RAM.

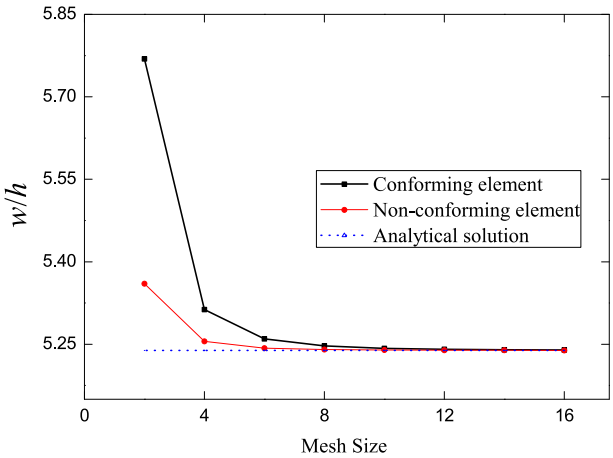

Fig. 3 Convergence study of conforming and non-conforming finite elements to calculate the transverse deflection of a passive simply supported micro-plate ($h = 11.01\mu$m, $a = b = 40h$, $l_0 = l_1 = l_2 = 11.01$ μm). Our FEM results agree well with analytical results presented in Akgoz and Civalek [42]

4.2 Analysis of flexoelectric composite plate under applied mechanical load: sensor mode

In what follows, the flexoelectric composite plate shown in Fig. 1 is analyzed under transverse mechanical load. The following material properties are used in the simulation:

- Flexoelectric material [62]: c_f= 139 GPa, v_f =0.3, f_1 =f_2 =1×10^{-6} C/m, ϵ =1×10^{-9} F/m;
- Passive material (Aluminum): c_p = 70 GPa, v_p =0.3.

where c_p, c_f denote Young's moduli of passive and flexoelectric layers, v_p, v_f denote the Poisson's ratios of passive and flexoelectric layers, f_1, f_2 denote the flexoelectric coefficients, and ϵ denotes the electric permittivity. The converse flexoelectric constants h_1, h_2 and direct flexoelectric constants f_1, f_2 are considered to be equal in the present analysis [63]. The value of mechanical length scale parameters $l_0 = l_1 = l_2$ is taken as 2 μm [62]. Ren and Sun [17] observed an enhanced electric permittivity of the material at microscale (similar to mechanical stiffness). The electric length scale parameters l_0^e, l_1^e are thus defined to incorporate lower scale effects through a higher-order permittivity term. In this work, the values of electric length scale parameters are considered to be equal to the mechanical length scale parameters, i.e., $l_0^e = l_1^e$ =2 μm [39].

The sensor response is now analyzed by solving for potential difference generated across the thickness of the plate for a given mechanical load input. The solution is obtained in terms of the nondimensional potential $\overline{\Phi}$ defined as

$$\overline{\Phi} = \phi \left(\frac{10^3 c_0 \epsilon_1 h^2}{q_0 f_2 a^2} \right), \tag{96}$$

where c_0=1 GPa is the scale for Young's modulus of the material and q_0 represents the magnitude of the applied mechanical load.

Firstly, the flexoelectric composite plate is analyzed under a uniformly distributed load $q_0 = -1$ N/m^2 and simply supported boundary conditions on all four edges. The potential difference generated across the flexoelectric layer at the center of the plate, i.e., at $\overline{\Phi}(a/2, b/2, h/2)$, is calculated. Potential boundary conditions (93)–(94) are assumed on all the edges of the plate. The total thickness of the composite plate h is taken as 2 μm; span-to-thickness ratio a/h is taken as 100, and thickness of flexoelectric layer h_f is taken as $0.5h$. Firstly, a convergence study is performed for both conforming and non-conforming elements, and the results are compared with analytical results in Fig. 4. The FEM results agree well with analytical results, and an error of 0.0041 % is noted between them. It may be observed that the conforming element shows a monotonic convergence, while the non-conforming element does not converge monotonically to the exact value. The computational time taken by the non-conforming finite element is 12.18 s, while the conforming element takes 22.59 s for a mesh size of 16 × 16. This demonstrates the computational efficiency of the non-conforming element.

The results in the following examples are presented for a mesh size of 16 × 16 using non-conforming finite element. Contour plots of the nondimensional potential $\overline{\Phi}$ for the different boundary conditions (SSSS, SCSS,

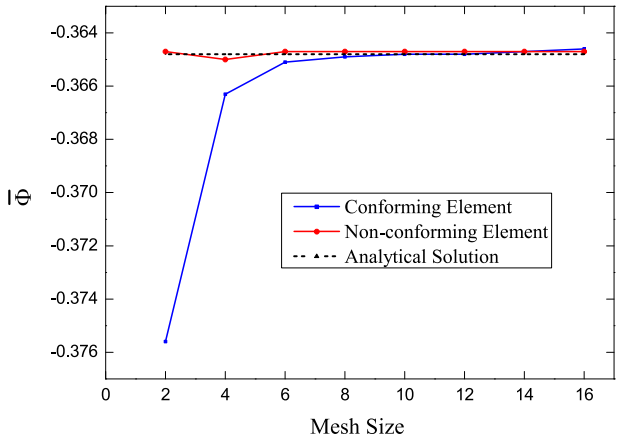

Fig. 4 Convergence study for calculation of nondimensional potential $\overline{\Phi}(a/2, b/2, h/2)$ with increasing mesh size (square mesh) for simply supported boundary conditions. The computational time taken by non-conforming finite element is 12.18 s, while the conforming element takes 22.59 s for 16 × 16 mesh size

SSSC, SCSC, FCFC, FFFC) are presented in Fig. 5. For a simply supported plate operating in sensor mode, $\overline{\Phi}$ is maximum at the center of the plate due to symmetric loading and geometry, and the strain gradients are also maximum at the center of the plate. For other boundary conditions, the maximum potential is observed near clamped edges as the strain gradients are also maximum at clamped edges. Moreover, the maximum potential is noted for FFFC boundary conditions.

Furthermore, the electrostatic potential developed across the flexoelectric layer due to an applied mechanical load has contributions from both direct and converse flexoelectric effects. Flexoelectric response due to the converse effect is compared with the response due to the direct effect for different thickness values of single edge clamped (FFFC), i.e., cantilever flexoelectric square plate ($a = b = 100\,h$, $h_f/h = 0.5$) subjected to a uniformly distributed load. The results are presented in Fig. 6 for two cases: (1) considering both direct and converse flexoelectric effects ($h_1 = h_2 = f_1 = f_2$) and (2) considering only direct flexoelectric effect and neglecting converse flexoelectric effect ($h_1 = h_2 = 0$). It is observed that not considering the converse effect results in a error of up to 25%, especially for a plate with thickness larger than 10 μm.

In what follows, the effective piezoelectric coefficient of the flexoelectric material is calculated using the formula $(d_{31})_{eff} = -\epsilon_1 E_3/T_{11}$ for open-circuit conditions at the clamped edge of the cantilever flexoelectric plate. The values are compared with the piezoelectric coefficient of Quartz for different thickness values in Fig. 7.

It is observed that the effective piezoelectric coefficient increases significantly for smaller thickness values. However, the value of d_{31} should be independent of its structural thickness in a piezoelectric material [23]. It has been observed by Abdollahi et al. [23] that at smaller thickness (of the order of a few microns), atomic force microscopy measurements in piezoelectric materials resulted in much larger piezoelectric coefficient values. This anomaly can be explained by the results shown in Fig. 7, wherein the enhanced flexoelectric response at lower scales results in a larger potential output for the same applied force [16,24,25,41].

Now, the effect of electrical length scale parameters (l_0^e, l_1^e) on the sensor response of flexoelectric plate with FFFC boundary conditions is analyzed. It is subjected to UDL, and the nondimensional potential $\overline{\Phi}$ is evaluated at the center of clamped end (0, $b/2$, $h/2$). The size effects on the permittivity of the material are analyzed in terms of the l/h ratio, and the individual and combined effects of two length scale parameters (l_0^e, l_1^e) are presented in Fig. 8. It is observed that an increase in the l/h ratio results in a lower $\overline{\Phi}$. It is due to increase in the effective permittivity of the material at smaller scales, which was also observed in recent studies by Ren et al. [17]. Moreover, the size effects are prominent in case of l_1^e as compared to l_0^e.

Finally, the effect of flexoelectric layer thickness h_f on the output potential $\overline{\Phi}(0, b/2, h/2)$ is analyzed. Variation of nondimensional potential $\overline{\Phi}(0, b/2, h/2)$ with h_f/h is presented in Fig. 9 for a single edge clamped flexoelectric plate (FFFC) subjected to UDL. In this study, three different types of passive substrates are considered. The material properties of substrate 1 (Aluminum) are taken as c_p = 70 GPa, v_p =0.3 [64]; for substrate 2 (Zirconia), the material properties are taken as c_p = 151 GPa, v_p =0.3 [65]; and for substrate 3 (Alumina), the material properties are taken as c_p = 380 GPa, v_p =0.3 [64]. The maximum potential is observed for $h_f/h = 1$. Hence, a flexoelectric plate with no substrate layer is an optimum choice for sensor

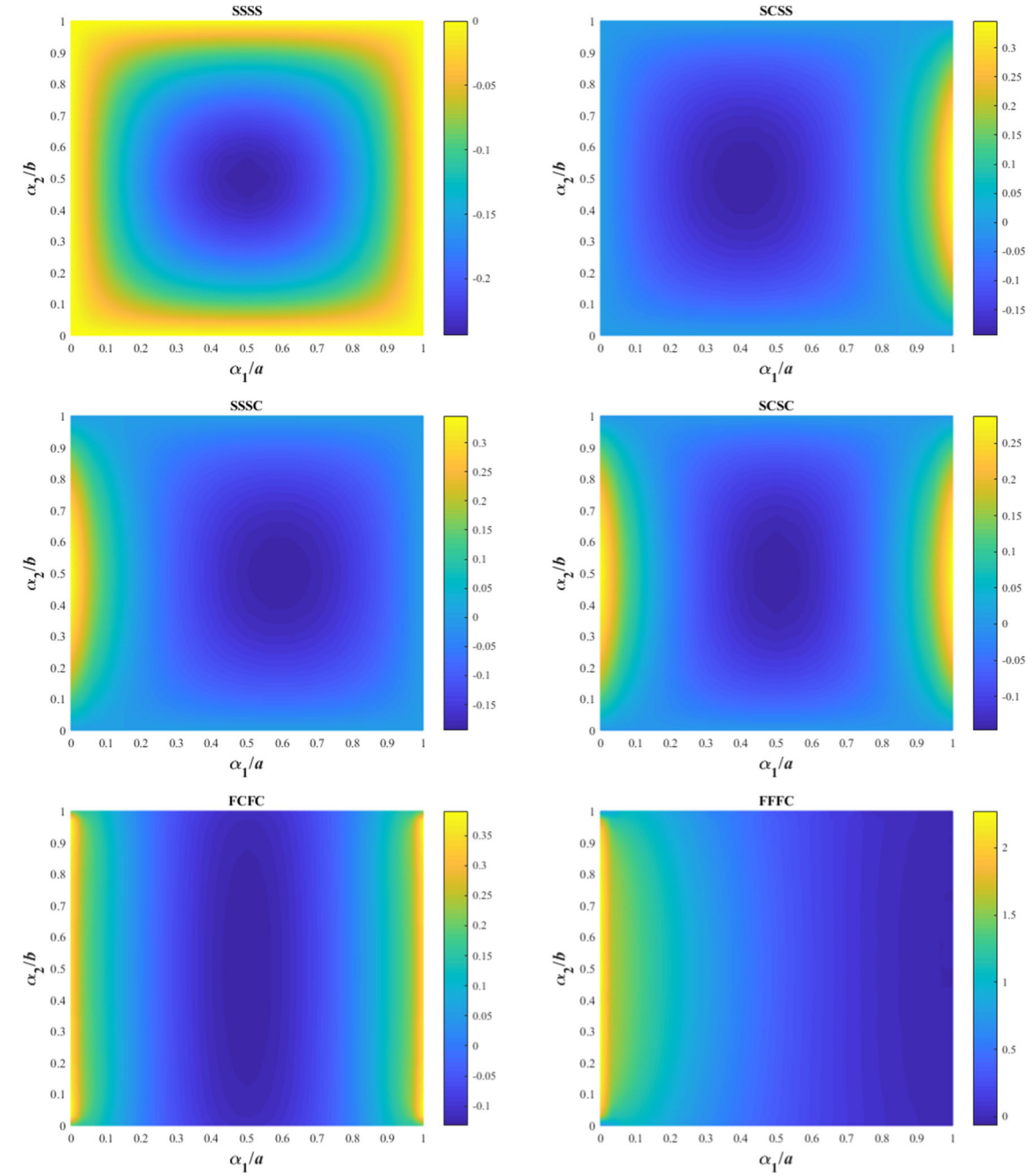

Fig. 5 Contour plots of potential $\overline{\Phi}$ at the mid-surface of a flexoelectric unimorph plate deforming under a uniformly distributed load, for different combination of boundary conditions ($h = 2\mu$m, $a = b = 100h$). For SSSS boundary conditions, $\overline{\Phi}$ is maximum at the center and in case of other boundary conditions, the maximum potential is observed near clamped edges. The maximum potential is noted at the clamped edge for FFFC boundary conditions

applications. In case of piezoelectric materials, in which electric field is coupled with bending stresses, the maximum potential is obtained for a piezoelectric layer thickness ratio in the range of 0.7−0.8 [66]. In case of a flexoelectric plate, the strain gradients G_{113} and G_{223} are constant across the thickness of the plate. Increase in thickness of the flexoelectric layer results in larger strain gradients, thus increasing the electrostatic potential generated across the flexoelectric layer.

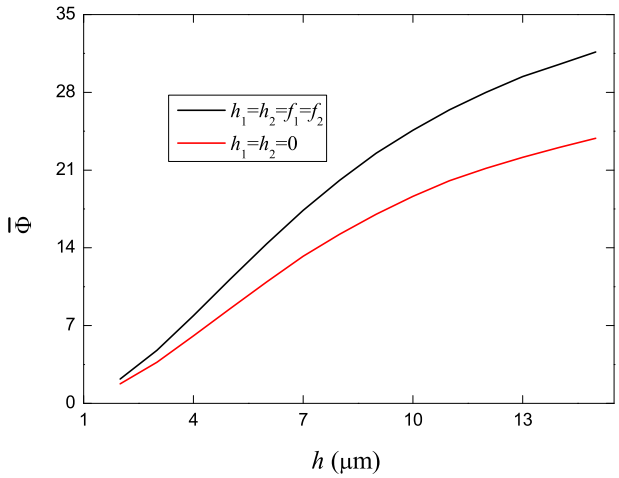

Fig. 6 Contribution of converse flexoelectric effect in the overall response of a cantilever flexoelectric square plate of thickness ratio $a/h = 100$ and $h_f/h = 0.5$ operating in the sensor mode. The converse flexoelectric effect gives rise to a larger effective response

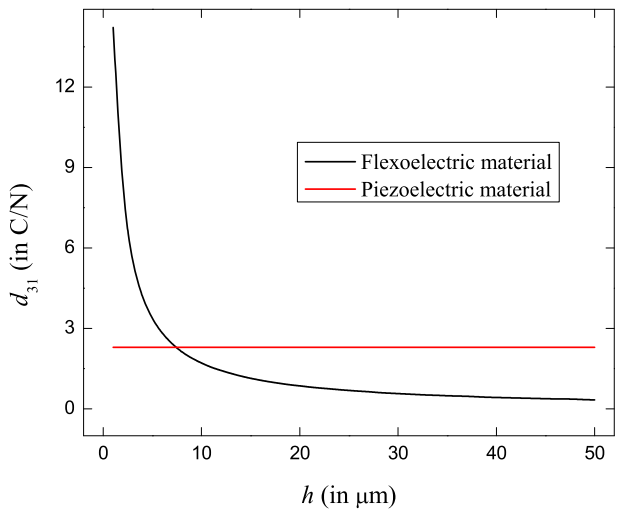

Fig. 7 Effective piezoelectric coefficient d_{31} for different flexoelectric layer thickness values in a square plate ($a = b, a = 100\,h$, $h_f/h = 1$). The value of effective piezoelectric coefficient is higher for flexoelectric material than piezoelectric materials for $h \leq 8$ μm. Similar effect has been observed in recent studies [23,24,35]

4.3 Analysis of flexoelectric composite plates under applied electrical load: actuator mode

We now analyze the flexoelectric composite plate in actuator mode, i.e., the deflection of the flexoelectric plate is evaluated under applied electrostatic potential. The actuator response is analyzed in terms of nondimensional deflection $\overline{w}$ defined by

$$\overline{w} = w_0 \left(\frac{10^4 f_2 h}{\Delta\phi \epsilon_1 a^2} \right), \tag{97}$$

where $\Delta\phi$ is the electrostatic potential applied across the flexoelectric layer. The flexoelectric actuator is analyzed for different boundary conditions (SSSS, SCSS, SCSC), and a uniform electrical potential ($\Delta\phi = 100$ V) is applied across the thickness of the flexoelectric layer. The results are presented in Table 1 for different mesh sizes. The FEM results for the non-conforming element are compared with the analytical solution for simply supported boundary conditions, and a good agreement is observed between them.

Contour plots of the nondimensional deflection $\overline{w}$ for the different boundary conditions (SSSS, SCSS, SSSC, SCSC, FCFC, FFFC) are presented in Fig. 10. For SSSS and SCSC boundary conditions, the maximum

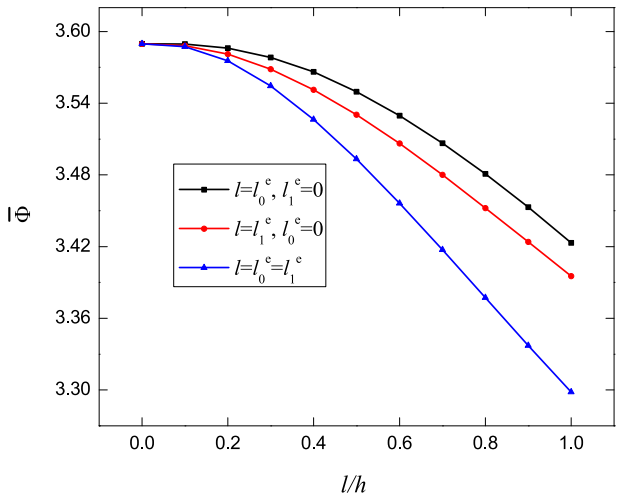

Fig. 8 Effect of electrical length scale parameter ratio l/h on nondimensional potential $\bar{\phi}$ developed in a cantilever flexoelectric plate. Increase in l/h ratio increases the higher-order permittivity of the material, which results in a decreased potential. Simulation results are shown for different length scale parameters in a uniformly loaded flexoelectric plate with $h = 2$ μm, $a = b = 100\,h$, $h_f/h = 1$

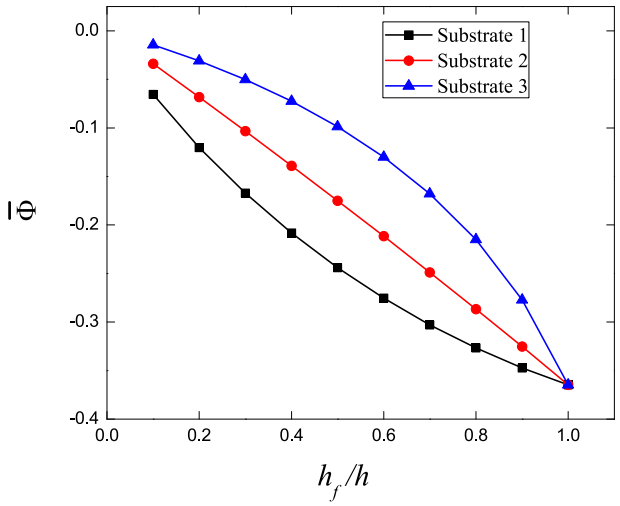

Fig. 9 Effect of flexoelectric layer thickness ratio h_f/h on the nondimensional potential $\overline{\Phi}$ of a cantilever flexoelectric square plate ($h = 2$ μm, $a = b = 100h$). The maximum potential is obtained for $h_f/h = 1$

Table 1 Nondimensional deflection $\overline{w} = w_0\left(\frac{10^4 f_2 h}{\Delta\phi_0 \epsilon_1 a^2}\right)$ for different boundary conditions. ($h = 2$ μm, $ab == 100\,h$, $\Delta\phi = 100$ V)

Mesh size	$h_f/h = 0.5$			$h_f/h = 1$		
	SSSS	SCSS	SCSC	SSSS	SCSS	SCSC
2 × 2	−1.2595	−0.8140	−0.4909	−0.9419	−0.6089	−0.3674
4 × 4	−1.2254	−0.6741	−0.2955	−0.9165	−0.5042	−0.2211
8 × 8	−1.2217	−0.6531	−0.2667	−0.9137	−0.4885	−0.1995
16 × 16	−1.2213	−0.6504	−0.2630	−0.9134	−0.4864	−0.1967
24 × 24	−1.2213	−0.6501	−0.2626	−0.9134	−0.4863	−0.1964
28 × 28	−1.2212	−0.6501	−0.2626	−0.9134	−0.4862	−0.1964
32 × 32	−1.2212	−0.6501	−0.2626	−0.9134	−0.4862	−0.1964
Analytical	−1.2212	–	–	−0.9134	–	–

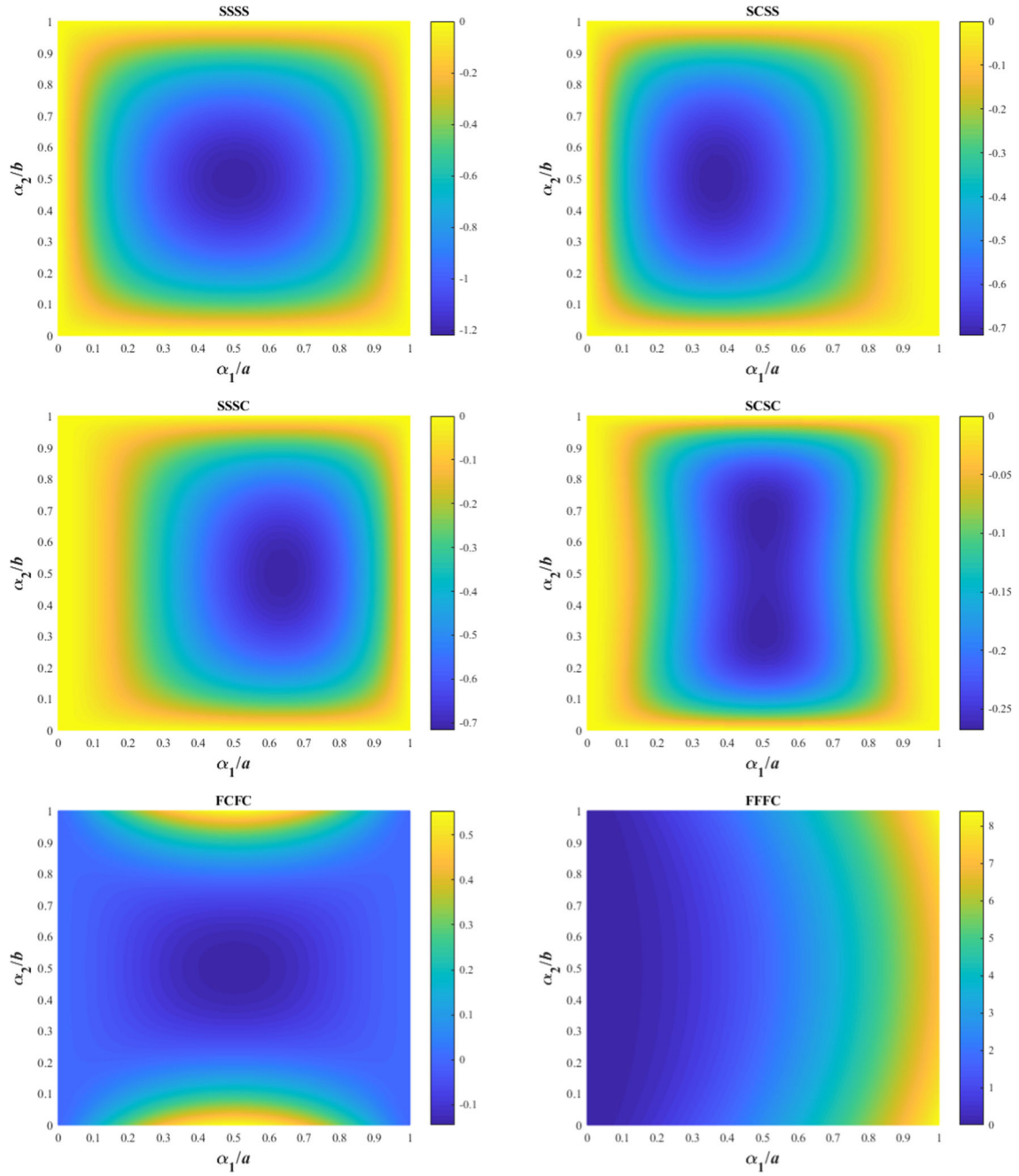

Fig. 10 Contour plots of nondimensional deflection $\overline{w}$ of a flexoelectric unimorph plate for various boundary conditions (h = 2 μm, $a = b = 100\,h$, $\Delta\phi = 100$ V, $h_f/h = 0.5$). The flexoelectric plate actuator deflects in -α_3 direction for SSSS, SCSS, SSSC, and SCSC boundary conditions, and deflection along +α_3 direction is observed on the free edges for FCFC and FFFC boundary conditions. Maximum deflection is observed for the flexoelectric plate with FFFC boundary conditions

deflection is observed at the center of the plate actuator due to symmetric boundary and loading conditions. It is noted that the actuator deflects in -α_3 direction for SSSS, SCSS, SSSC, and SCSC boundary conditions. On the other hand, deflection along +α_3 direction is observed on the free edges for FCFC and FFFC boundary conditions. Maximum deflection is observed on the free edge of the cantilever flexoelectric plate (with FFFC boundary conditions).

The three-dimensional contour plots of the nondimensional deflection w/h for cantilever flexoelectric plate are presented in Fig. 11. The flexoelectric actuator is subjected to different values of electrostatic potential ($\Delta\phi$),

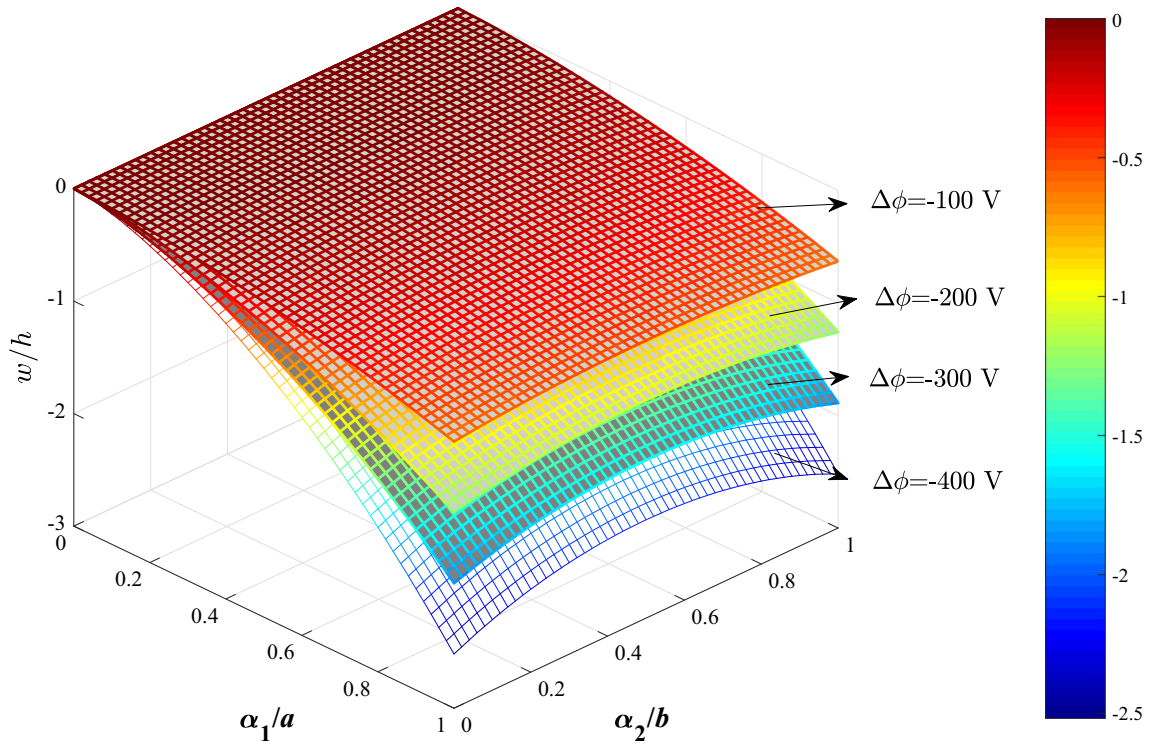

Fig. 11 Deformation contour plots for a flexoelectric plate clamped at one edge (cantilever) under applied electrostatic potential

and it is observed that actuator deflection increases with increase in potential difference applied across the flexoelectric layer.

Next, the actuator response of a simply supported flexoelectric plate is analyzed for different thickness values. The different values of plate thickness h are taken as 2 μm and 80 μm. Variation of nondimensional deflection $\overline{w}$ along α_1/a ($\alpha_2 = b/2$) is presented for classical theory ($l_0 = l_1 = l_2 = 0$, $l_0^e = l_1^e$= 2 μm), modified couple stress theory ($l_0 = l_1 = 0$, l_2= 2 μm, $l_0^e = l_1^e$= 2 μm) and strain gradient theory ($l_0 = l_1 = l_2$= 2 μm, $l_0^e = l_1^e$= 2 μm) in Fig. 12. A considerable difference is noted among the results of these theories for lower thickness value, i.e., h = 2 μm. There is a negligible difference between the results of the three theories for h = 80 μm, as size effects become negligible with increasing thickness.

We now study the effect of the mechanical length scale parameters on the actuator response of a flexoelectric plate with FFFC boundary conditions. The flexoelectric plate is subjected to uniform electrostatic potential load ($\Delta\Phi$=100 V). The maximum deflection at the free edge ($\alpha_1 = a$) of flexoelectric plate is calculated. The effect on the actuator response is analyzed in terms of length scale-to-thickness ratio l/h, and the individual effects of three mechanical length scale parameters (l_0, l_1 and l_2) are presented in Fig. 13. The increase in the l/h ratio increases the effective stiffness of the flexoelectric actuator, which leads to a decrease in the nondimensional deflection. The size effects are prominently influenced by length scale parameter l_0 as compared to l_1 and l_2. In this study, the values of length scale parameters are considered to be equal. However, different values of these parameters can be chosen to better fit the experimental results. The strain gradient theory gives the choice of three length scale parameters (l_0, l_1, l_2), which makes it more versatile compared to modified couple stress theory, which considers only one length scale parameter l_2.

As the last example of this section, the effect of flexoelectric layer thickness h_f on the actuator response is analyzed in terms of thickness ratio h_f/h. In this study, three passive substrates were considered, namely aluminum, zirconia, and alumina. A uniform electrostatic potential difference ($\Delta\Phi$=100 V) is applied across the flexoelectric layer. Variation of the nondimensional deflection $\overline{w}$ with h_f/h is presented in Fig. 14. It is noted that the flexoelectric plate with substrate 1 shows a decrease in the nondimensional deflection with the increase in the layer thickness ratio. However, the nondimensional deflection increases for the flexoelectric plates having substrate 2 and substrate 3 with the increase in the thickness ratio. This is due to the fact that the stiffness of substrate 1 made of aluminum is lesser than that of flexoelectric material. With the increase in

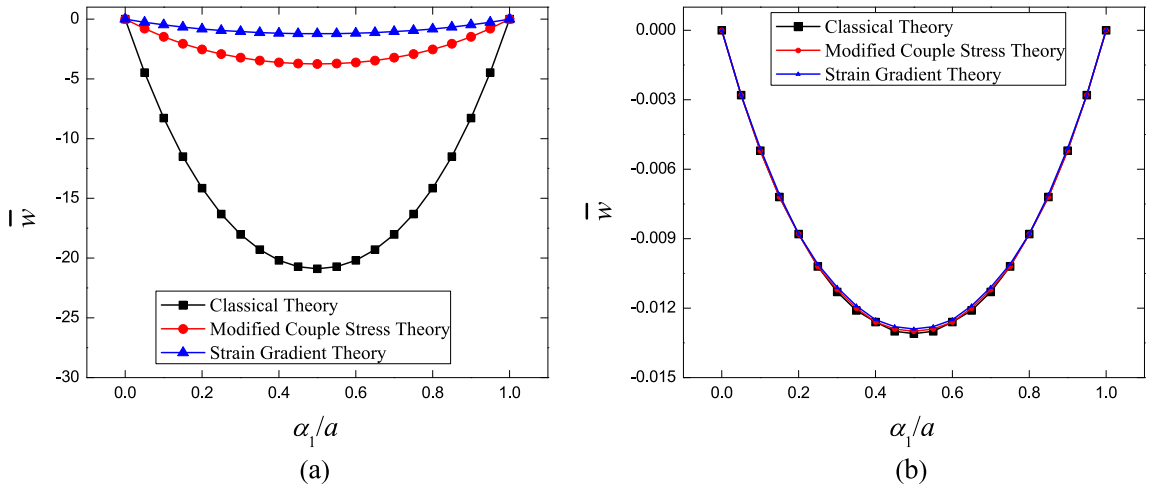

Fig. 12 Effect of plate thickness on nondimensional deflection $\overline{w}$ of a simply supported flexoelectric composite plate ($h_f/h = 0.5$): **a** h=2 μm, **b** h=80 μm. It can be clearly seen that higher-order theories do not give significantly different results for a plate of thickness h=80 μm (or more). However, a considerable difference among the results of classical theory, modified couple stress theory, and strain gradient theory is noted at 2μm due to size effects

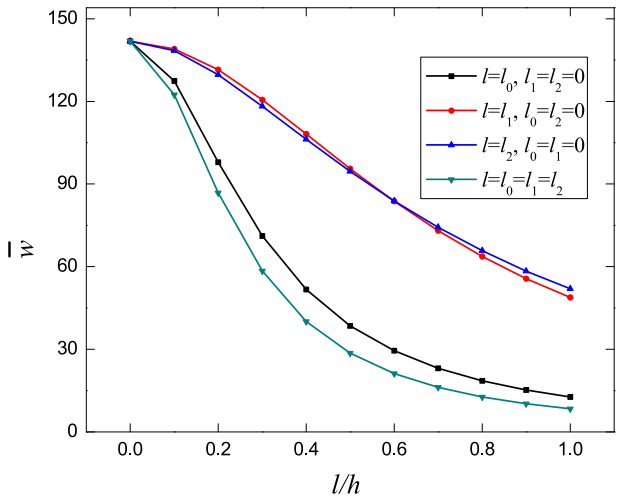

Fig. 13 Effect of mechanical length scale parameters on nondimensional deflection $\overline{w}(a, b/2)$ for a cantilever flexoelectric plate. The length scale parameter l_0 incorporates size effects more prominently as compared to l_1 and l_2 (h = 2 μm, $a = b = 100\,h$, $h_f/h = 0.5$)

the thickness ratio, the flexural rigidity of the plate increases, which leads to a decrease in the deflection. On the contrary, the flexural rigidity of the plate with substrate 2 and substrate 3 decreases with an increase in the thickness ratio, which increases the actuator deflection.

5 Conclusions

This work presents the development of a two-way coupled flexoelectric plate formulation starting from a 3D gradient electromechanical theory. This theory considers both direct and converse flexoelectric effects along with the mechanical and electrical size effects at microscale. A 2D theory for flexoelectric plates is derived using the variational formulation by considering Kirchhoff assumptions. A computationally efficient C^2 continuous non-conforming finite element framework is developed to solve the resulting plate equations. The finite element is implemented to analyze the sensor and actuator response of flexoelectric plates for different thickness scales. A Navier-type analytical solution is also derived to verify the accuracy of the finite element results. Our finite element results are also validated with experimental results from literature, for a passive

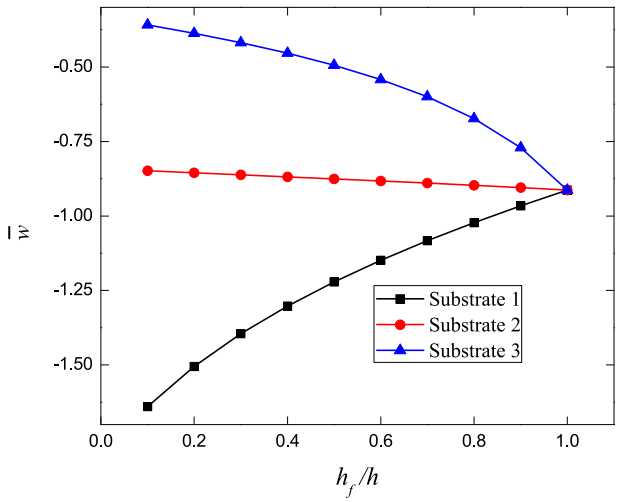

Fig. 14 Effect of flexoelectric layer thickness ratio h_f/h on the nondimensional tip deflection $\overline{w}$ of a cantilever flexoelectric plate ($h = 2$ μm, $a = b = 100h$). The nondimensional deflection is dependent on the choice of the substrate

micro-plate. A number of examples are considered to study the effect of different parameters on actuator and sensor response of flexoelectric plates, and the following observations are made:

- The non-conforming element is nearly two times faster than the conforming element for a mesh size of 16 × 16.
- Flexoelectric response of dielectric materials increases significantly at microscale, and it is larger than the electromechanical response of piezoelectric materials for a plate of thickness $h \leq 8$ μm.
- The influence of mechanical and electrical length scale parameters on the sensor and actuator response of flexoelectric plates is examined. The mechanical length scale parameters describe the increase in material stiffness at lower scales, and electrical length scale parameters account for the increase in dielectric permittivity at microscale.
- The actuator response of flexoelectric composite plates depends on the stiffness of the passive substrate. A substrate having lesser stiffness can be used for larger actuation. On the other hand, the maximum voltage output of flexoelectric plate sensors is obtained for flexoelectric layer thickness ratio $h_f/h = 1$ (i.e., no substrate layer).

Appendix A

Components of constitutive matrices: The components of $\overline{\mathbf{H}}$, $\overline{\mathbf{G}}$, $\overline{\mathbf{D}}$, $\overline{\mathbf{E}}$, $\overline{\mathbf{B}}$ and $\overline{\mathbf{K}}$ matrices defined in equations (51)–(54) are given as follows:

$$\overline{\mathbf{H}} = \begin{bmatrix} H_{111} & H_{112} & H_{113} & H_{221} & H_{222} & H_{223} & H_{121} & H_{122} & H_{123} \end{bmatrix}^{\mathrm{T}}, \tag{98}$$

$$\overline{\mathbf{G}} = \begin{bmatrix} G_{111} & G_{112} & G_{113} & G_{221} & G_{222} & G_{223} & G_{121} & G_{122} & G_{123} \end{bmatrix}^{\mathrm{T}}, \tag{99}$$

$$\overline{\mathbf{D}} = \begin{bmatrix} D_1 & D_2 & D_3 \end{bmatrix}^{\mathrm{T}}, \quad \overline{\mathbf{E}} = \begin{bmatrix} E_1 & E_2 & E_3 \end{bmatrix}^{\mathrm{T}}, \tag{100}$$

$$\overline{\mathbf{B}} = \begin{bmatrix} B_{11} & B_{22} & B_{33} & B_{12} & B_{13} & B_{23} \end{bmatrix}^{\mathrm{T}}, \tag{101}$$

$$\overline{\mathbf{K}} = \begin{bmatrix} K_{11} & K_{22} & K_{33} & K_{12} & K_{13} & K_{23} \end{bmatrix}^{\mathrm{T}}. \tag{102}$$

The components of material matrices $\overline{\mathbf{Q}}^{\mathbf{c}}$, $\overline{\mathbf{Q}}^{\mathbf{g}}$, $\overline{\boldsymbol{\epsilon}}$, $\overline{\mathbf{k}}$, $\overline{\mathbf{h}}$ and $\overline{\mathbf{f}}$ defined in Eqs. (51)–(54) are given by:

$$\overline{\mathbf{Q}}^{\mathbf{c}} = \begin{bmatrix} \overline{Q}^c_{11} & \overline{Q}^c_{12} & 0 \\ \overline{Q}^c_{21} & \overline{Q}^c_{22} & 0 \\ 0 & 0 & \overline{Q}^c_{33} \end{bmatrix}, \tag{103}$$

where $\overline{Q}^{c}_{ij}$, $i, j = 1, 2, 3$ are the components of stiffness matrix and can be obtained in terms of Young's modulus c and Poison's ratio v using the plane stress assumptions [42].

$$\overline{\mathbf{h}} = \begin{bmatrix} h_1 + 2h_2 & h_1 & h_1 & 0 & 0 & 0 \\ h_1 & h_1 + 2h_2 & h_1 & 0 & 0 & 0 \\ 0 & 0 & 0 & 2h_2 & 0 & 0 \end{bmatrix}, \tag{104}$$

$$\overline{\mathbf{Q}}^{\mathbf{g}} = \begin{bmatrix} \overline{Q}^{g}_{11} & 0 & 0 & \overline{Q}^{g}_{14} & 0 & 0 & 0 & \overline{Q}^{g}_{18} & 0 \\ 0 & \overline{Q}^{g}_{22} & 0 & 0 & \overline{Q}^{g}_{25} & 0 & \overline{Q}^{g}_{27} & 0 & 0 \\ 0 & 0 & \overline{Q}^{g}_{33} & 0 & 0 & \overline{Q}^{g}_{36} & 0 & 0 & 0 \\ \overline{Q}^{g}_{41} & 0 & 0 & \overline{Q}^{g}_{44} & 0 & 0 & 0 & \overline{Q}^{g}_{48} & 0 \\ 0 & \overline{Q}^{g}_{52} & 0 & 0 & \overline{Q}^{g}_{55} & 0 & \overline{Q}^{g}_{57} & 0 & 0 \\ 0 & 0 & \overline{Q}^{g}_{63} & 0 & 0 & \overline{Q}^{g}_{66} & 0 & 0 & 0 \\ 0 & \overline{Q}^{g}_{72} & 0 & 0 & \overline{Q}^{g}_{75} & 0 & \overline{Q}^{g}_{77} & 0 & 0 \\ \overline{Q}^{g}_{81} & 0 & 0 & \overline{Q}^{g}_{84} & 0 & 0 & 0 & \overline{Q}^{g}_{88} & 0 \\ 0 & 0 & 0 & 0 & 0 & 0 & 0 & 0 & \overline{Q}^{g}_{99} \end{bmatrix}, \tag{105}$$

where $\overline{Q}^{g}_{11} = 2(a_1 + a_2 + a_3 + a_4 + a_5)$, $\overline{Q}^{g}_{14} = 2a_1 + a_2$, $\overline{Q}^{g}_{18} = a_3 + \frac{1}{2}a_2$, $\overline{Q}^{g}_{22} = 2a_1 + 2a_4$, $\overline{Q}^{g}_{25} = \overline{Q}^{g}_{14}$, $\overline{Q}^{g}_{27} = \frac{1}{2}a_2 + a_5$, $\overline{Q}^{g}_{33} = \overline{Q}^{g}_{22}$, $\overline{Q}^{g}_{36} = 2a_1$, $\overline{Q}^{g}_{41} = \overline{Q}^{g}_{14}$, $\overline{Q}^{g}_{44} = \overline{Q}^{g}_{22}$, $\overline{Q}^{g}_{48} = \overline{Q}^{g}_{27}$, $\overline{Q}^{g}_{52} = \overline{Q}^{g}_{25}$, $\overline{Q}^{g}_{55} = \overline{Q}^{g}_{11}$, $\overline{Q}^{g}_{57} = \overline{Q}^{g}_{18}$, $\overline{Q}^{g}_{63} = \overline{Q}^{g}_{36}$, $\overline{Q}^{g}_{66} = \overline{Q}^{g}_{33}$, $\overline{Q}^{g}_{72} = \overline{Q}^{g}_{27}$, $\overline{Q}^{g}_{75} = \overline{Q}^{g}_{57}$, $\overline{Q}^{g}_{77} = a_3 + 2a_4 + a_5$, $\overline{Q}^{g}_{81} = \overline{Q}^{g}_{18}$, $\overline{Q}^{g}_{84} = \overline{Q}^{g}_{48}$, $\overline{Q}^{g}_{88} = \overline{Q}^{g}_{77}$ and $\overline{Q}^{g}_{99} = 2a_4$.

$$\overline{\mathbf{f}} = \begin{bmatrix} 2f_1 + f_2 & 0 & 0 \\ 0 & f_2 & 0 \\ 0 & 0 & f_2 \\ f_2 & 0 & 0 \\ 0 & 2f_1 + f_2 & 0 \\ 0 & 0 & f_2 \\ 0 & f_1 & 0 \\ f_1 & 0 & 0 \\ 0 & 0 & 0 \end{bmatrix}, \tag{106}$$

$$\overline{\boldsymbol{\epsilon}} = \begin{bmatrix} \epsilon_1 & 0 & 0 \\ 0 & \epsilon_1 & 0 \\ 0 & 0 & \epsilon_1 \end{bmatrix}, \tag{107}$$

and

$$\overline{\mathbf{k}} = \begin{bmatrix} k_1 + 2k_2 & k_1 & k_1 & 0 & 0 & 0 \\ k_1 & k_1 + 2k_2 & k_1 & 0 & 0 & 0 \\ k_1 & k_1 & k_1 + 2k_2 & 0 & 0 & 0 \\ 0 & 0 & 0 & 2k_2 & 0 & 0 \\ 0 & 0 & 0 & 0 & 2k_2 & 0 \\ 0 & 0 & 0 & 0 & 0 & 2k_2 \end{bmatrix}. \tag{108}$$

Appendix B

The matrices $\mathbf{D^{SS}}$, $\mathbf{D^{SK}}$, $\mathbf{D^{GG}}$, $\mathbf{D^{GE}}$, $\mathbf{D^{EE}}$, $\mathbf{D^{EG}}$, $\mathbf{D^{KK}}$ and $\mathbf{D^{KS}}$ defined in Eq. (84) are given by:

$$\mathbf{D^{SS}} = \int_{\alpha_3} (\mathbf{H^S})^{\mathrm{T}} \overline{\mathbf{Q}}^{\mathbf{c}} \mathbf{H^S} \mathrm{d}\alpha_3, \tag{109}$$

$$\mathbf{D^{SK}} = \int_{\alpha_3} (\mathbf{H^S})^{\mathrm{T}} \overline{\mathbf{h}} \mathbf{H^K} \mathrm{d}\alpha_3, \tag{110}$$

$$\mathbf{D^{GG}} = \int_{\alpha_3} (\mathbf{H^G})^{\mathrm{T}} \overline{\mathbf{Q}}^{\mathbf{g}} \mathbf{H^G} \mathrm{d}\alpha_3, \tag{111}$$

$$\mathbf{D^{GE}} = \int_{\alpha_3} (\mathbf{H^G})^{\mathrm{T}} \bar{\mathbf{f}} \mathbf{H^E} \mathrm{d}\alpha_3, \tag{112}$$

$$\mathbf{D^{EE}} = \int_{\alpha_3} (\mathbf{H^E})^{\mathrm{T}} \bar{\boldsymbol{\epsilon}} \mathbf{H^E} \mathrm{d}\alpha_3, \tag{113}$$

$$\mathbf{D^{EG}} = \int_{\alpha_3} (\mathbf{H^E})^{\mathrm{T}} \bar{\mathbf{f}}^{\mathrm{T}} \mathbf{H^G} \mathrm{d}\alpha_3, \tag{114}$$

$$\mathbf{D^{KK}} = \int_{\alpha_3} (\mathbf{H^K})^{\mathrm{T}} \bar{\mathbf{k}} \mathbf{H^K} \mathrm{d}\alpha_3. \tag{115}$$

$$\mathbf{D^{KS}} = \int_{\alpha_3} (\mathbf{H^K})^{\mathrm{T}} \bar{\mathbf{h}}^{\mathrm{T}} \mathbf{H^S} \mathrm{d}\alpha_3, \tag{116}$$

The finite element matrices $\mathbf{K^{SS}}$, $\mathbf{K^{SK}}$, $\mathbf{K^{GG}}$, $\mathbf{K^{GE}}$, $\mathbf{K^{EE}}$, $\mathbf{K^{EG}}$, $\mathbf{K^{KK}}$ and $\mathbf{K^{KS}}$ defined in Eq. (85) are given by:

$$\mathbf{K^{SS}} = \int_{\alpha_1^e} \int_{\alpha_2^e} (\mathbf{B^S})^{\mathrm{T}} \mathbf{D^{SS}} \mathbf{B^S} \mathrm{d}\alpha_2^e \mathrm{d}\alpha_1^e, \tag{117}$$

$$\mathbf{K^{SK}} = \int_{\alpha_1^e} \int_{\alpha_2^e} (\mathbf{B^S})^{\mathrm{T}} \mathbf{D^{SK}} \mathbf{B^K} \mathrm{d}\alpha_2^e \mathrm{d}\alpha_1^e, \tag{118}$$

$$\mathbf{K^{GG}} = \int_{\alpha_1^e} \int_{\alpha_2^e} (\mathbf{B^G})^{\mathrm{T}} \mathbf{D^{GG}} \mathbf{B^G} \mathrm{d}\alpha_2^e \mathrm{d}\alpha_1^e, \tag{119}$$

$$\mathbf{K^{GE}} = \int_{\alpha_1^e} \int_{\alpha_2^e} (\mathbf{B^G})^{\mathrm{T}} \mathbf{D^{GE}} \mathbf{B^E} \mathrm{d}\alpha_2^e \mathrm{d}\alpha_1^e, \tag{120}$$

$$\mathbf{K^{EE}} = \int_{\alpha_1^e} \int_{\alpha_2^e} (\mathbf{B^E})^{\mathrm{T}} \mathbf{D^{EE}} \mathbf{B^E} \mathrm{d}\alpha_2^e \mathrm{d}\alpha_1^e, \tag{121}$$

$$\mathbf{K^{EG}} = \int_{\alpha_1^e} \int_{\alpha_2^e} (\mathbf{B^E})^{\mathrm{T}} \mathbf{D^{EG}} \mathbf{B^G} \mathrm{d}\alpha_2^e \mathrm{d}\alpha_1^e, \tag{122}$$

$$\mathbf{K^{KK}} = \int_{\alpha_1^e} \int_{\alpha_2^e} (\mathbf{B^K})^{\mathrm{T}} \mathbf{D^{KK}} \mathbf{B^K} \mathrm{d}\alpha_2^e \mathrm{d}\alpha_1^e, \tag{123}$$

$$\mathbf{K^{KS}} = \int_{\alpha_1^e} \int_{\alpha_2^e} (\mathbf{B^K})^{\mathrm{T}} \mathbf{D^{KS}} \mathbf{B^S} \mathrm{d}\alpha_2^e \mathrm{d}\alpha_1^e, \tag{124}$$

Appendix C

Analytical solution for simply supported flexoelectric composite plates: The derived governing equations for the classical flexoelectric plate are solved analytically for simply supported boundary conditions. The governing differential equations (62)–(66) are obtained in the explicit form using Eqs. (58)–(61). The Navier solution is used to express the primary variables in terms of series solution as follows:

$$u_0 = \sum_{m=1}^{\infty} \sum_{n=1}^{\infty} U_{mn} \cos(p\alpha_1) \sin(l\alpha_2), \tag{125}$$

$$v_0 = \sum_{m=1}^{\infty} \sum_{n=1}^{\infty} V_{mn} \sin(p\alpha_1) \cos(l\alpha_2), \tag{126}$$

$$w_0 = \sum_{m=1}^{\infty} \sum_{n=1}^{\infty} W_{mn} \sin(p\alpha_1) \sin(l\alpha_2), \tag{127}$$

$$\phi_1 = \sum_{m=1}^{\infty} \sum_{n=1}^{\infty} \Phi_{mn} \sin(p\alpha_1) \sin(l\alpha_2), \tag{128}$$

$$\phi_0 = \sum_{m=1}^{\infty}\sum_{n=1}^{\infty}\gamma_{mn}\sin(p\alpha_1)\sin(l\alpha_2), \tag{129}$$

where $p = \pi m/a$ and $l = \pi n/b$. The coefficients U_{mn}, V_{mn}, W_{mn}, Φ_{mn} and γ_{mn} are unknowns to be solved using the Navier solution technique.
In addition, transverse load $q(\alpha_1, \alpha_2)$ is expressed in terms of Fourier series as

$$q = \sum_{m=1}^{\infty}\sum_{n=1}^{\infty}q_{mn}\sin(p\alpha_1)\sin(l\alpha_2), \tag{130}$$

where

$$q_{mn} = \frac{4}{ab}\int_0^b\int_0^a q(\alpha_1, \alpha_2)\sin(p\alpha_1)\sin(l\alpha_2)\,\mathrm{d}\alpha_1\mathrm{d}\alpha_2, \tag{131}$$

The series solutions (125)–(130) are substituted into the explicit form of governing equations, resulting in algebraic equations of the form:

$$\mathbf{R^g U^g} = \mathbf{F^g}, \tag{132}$$

where $\mathbf{U^g}$ is the vector of unknowns to be solved, which is given by

$$\mathbf{U^g} = \left[U_{mn}\ V_{mn}\ W_{mn}\ \Phi_{mn}\ \gamma_{mn}\right]^{\mathrm{T}},$$

$\mathbf{F^g}$ is the resultant force matrix, and $\mathbf{R^g}$ is the 5×5 resultant stiffness matrix. Equation (132) is solved to obtain the displacements and electrostatic potential in terms of Navier coefficients. This general formulation is used to analyze the flexoelectric plate, both in actuator and sensor modes.

References

1. Wang, B., Gu, Y., Zhang, S., Chen, L.-Q.: Flexoelectricity in solids: progress, challenges, and perspectives. Prog. Mater. Sci. **106**, 100570 (2019)
2. Deng, Q., Liu, L., Sharma, P.: A continuum theory of flexoelectricity. In: Flexoelectricity in Solids: From Theory to Applications, pp. 111–167. World Scientific (2017)
3. Majdoub, M., Sharma, P., Cagin, T.: Enhanced size-dependent piezoelectricity and elasticity in nanostructures due to the flexoelectric effect. Phys. Rev. B **77**(12), 125424 (2008)
4. Gregg, J.M.: Stressing ferroelectrics. Science **336**(6077), 41–42 (2012)
5. Yan, Z., Jiang, L.: Flexoelectric effect on the electroelastic responses of bending piezoelectric nanobeams. J. Appl. Phys. **113**(19), 194102 (2013)
6. Zhuang, X., Nguyen, B.H., Nanthakumar, S.S., Tran, T.Q., Alajlan, N., Rabczuk, T.: Computational modeling of flexoelectricity—a review. Energies **13**(6), 1326 (2020)
7. Deng, B., Li, H., Tzou, H.: Optimal positions for multiple flexoelectric actuations on beams. In: ASME International Mechanical Engineering Congress and Exposition, vol. 57564, p. V013T16A008. American Society of Mechanical Engineers (2015)
8. Zhang, X., Yu, W., Fu, J., Tzou, H.: Flexoelectric control of beams with atomic force microscope probe excitation. Proc. Inst. Mech. Eng. C J. Mech. Eng. Sci. **234**(13), 2537–2549 (2020)
9. Hu, S., Li, H., Tzou, H.: Distributed flexoelectric structural sensing: theory and experiment. J. Sound Vib. **348**, 126–136 (2015)
10. Zhang, X., Li, H., Tzou, H.: Vibration control of a cantilever beam by metal-core flexoelectric and piezoelectric fibers. In: ASME 2014 International Mechanical Engineering Congress and Exposition. American Society of Mechanical Engineers Digital Collection (2014)
11. Merupo, V.I., Guiffard, B., Seveno, R., Tabellout, M., Kassiba, A.: Flexoelectric response in soft polyurethane films and their use for large curvature sensing. J. Appl. Phys. **122**(14), 144101 (2017)
12. Dai, H., Yan, Z., Wang, L.: Nonlinear analysis of flexoelectric energy harvesters under force excitations. Int. J. Mech. Mater. Des. **16**(1), 19–33 (2020)
13. Liu, C., Hu, S., Shen, S.: Effect of flexoelectricity on electrostatic potential in a bent piezoelectric nanowire. Smart Mater. Struct. **21**(11), 115024 (2012)
14. Deng, Q., Kammoun, M., Erturk, A., Sharma, P.: Nanoscale flexoelectric energy harvesting. Int. J. Solids Struct. **51**(18), 3218–3225 (2014)
15. Yang, W., Liang, X., Shen, S.: Electromechanical responses of piezoelectric nanoplates with flexoelectricity. Acta Mechanica **226**(9), 3097–3110 (2015)
16. Wang, K., Wang, B.: An analytical model for nanoscale unimorph piezoelectric energy harvesters with flexoelectric effect. Compos. Struct. **153**, 253–261 (2016)

17. Ren, H., Sun, W.-F.: Characterizing dielectric permittivity of nanoscale dielectric films by electrostatic micro-probe technology: finite element simulations. Sensors **19**(24), 5405 (2019)
18. Sahin, E., Dost, S.: A strain-gradients theory of elastic dielectrics with spatial dispersion. Int. J. Eng. Sci. **26**(12), 1231–1245 (1988)
19. Maranganti, R., Sharma, N., Sharma, P.: Electromechanical coupling in nonpiezoelectric materials due to nanoscale nonlocal size effects: Green's function solutions and embedded inclusions. Phys. Rev. B **74**(1), 014110 (2006)
20. Hu, S., Shen, S.: Variational principles and governing equations in nano-dielectrics with the flexoelectric effect. Sci. China Phys. Mech. Astron. **53**(8), 1497–1504 (2010)
21. Romeo, M.: Micromorphic continuum model for electromagnetoelastic solids. Z. Angew. Math. Phys. **62**(3), 513–527 (2011)
22. Romeo, M.: Polarization in dielectrics modeled as micromorphic continua. Z. Angew. Math. Phys. **66**(3), 1233–1247 (2015)
23. Abdollahi, A., Domingo, N., Arias, I., Catalan, G.: Converse flexoelectricity yields large piezoresponse force microscopy signals in non-piezoelectric materials. Nat. Commun. **10**(1), 1–6 (2019)
24. Joshan, Y.S., Santapuri, S.: A gradient electromechanical theory for thin dielectric curved beams considering direct and converse flexoelectric effects. Z. Angew. Math. Phys. **73**, 178 (2022)
25. Wang, K., Wang, B.: Non-linear flexoelectricity in energy harvesting. Int. J. Eng. Sci. **116**, 88–103 (2017)
26. Yue, Y., Xu, K., Chen, T.: A micro scale timoshenko beam model for piezoelectricity with flexoelectricity and surface effects. Compos. Struct. **136**, 278–286 (2016)
27. Sharma, S., Kumar, A., Kumar, R., Talha, M., Vaish, R.: Geometry independent direct and converse flexoelectric effects in functionally graded dielectrics: an isogeometric analysis. Mech. Mater. **148**, 103456 (2020)
28. Tian, X., Xu, M., Deng, Q., Sladek, J., Sladek, V., Repka, M., Li, Q.: Size-dependent direct and converse flexoelectricity around a micro-hole. Acta Mech. **231**(12), 4851–4865 (2020)
29. Sharma, S., Kumar, R., Talha, M., Vaish, R.: Strategies to instigate superior electromechanical response in dielectric materials via converse flexoelectricity. Extreme Mech. Lett. **42**, 101138 (2021)
30. Haque, M.F., Snapp, P., Kim, J.M., Wang, M.C., Bae, H.J., Cho, C., Nam, S.: Strongly enhanced electromechanical coupling in atomically thin transition metal dichalcogenides. Mater. Today **47**, 69–74 (2021)
31. Zhang, Z., Yan, Z., Jiang, L.: Flexoelectric effect on the electroelastic responses and vibrational behaviors of a piezoelectric nanoplate. J. Appl. Phys. **116**(1), 014307 (2014)
32. Li, A., Zhou, S., Qi, L.: Size-dependent electromechanical coupling behaviors of circular micro-plate due to flexoelectricity. Appl. Phys. A **122**(10), 1–18 (2016)
33. Ebrahimi, F., Barati, M.R.: Vibration analysis of size-dependent flexoelectric nanoplates incorporating surface and thermal effects. Mech. Adv. Mater. Struct. **25**(7), 611–621 (2018)
34. Qi, L., Huang, S., Fu, G., Li, A., Zhou, S., Jiang, X.: Modeling of the flexoelectric annular microplate based on strain gradient elasticity theory. Mech. Adv. Mater. Struct. **26**(23), 1958–1968 (2019)
35. Chen, L., Pan, S., Fei, Y., Zhang, W., Yang, F.: Theoretical study of micro/nano-scale bistable plate for flexoelectric energy harvesting. Appl. Phys. A **125**(4), 1–11 (2019)
36. Amir, S., BabaAkbar-Zarei, H., Khorasani, M.: Flexoelectric vibration analysis of nanocomposite sandwich plates. Mech. Based Des. Struct. Mach. **48**(2), 146–163 (2020)
37. Abdollahi, A., Peco, C., Millan, D., Arroyo, M., Arias, I.: Computational evaluation of the flexoelectric effect in dielectric solids. J. Appl. Phys. **116**(9), 093502 (2014)
38. Abdollahi, A., Millán, D., Peco, C., Arroyo, M., Arias, I.: Revisiting pyramid compression to quantify flexoelectricity: a three-dimensional simulation study. Phys. Rev. B **91**(10), 104103 (2015)
39. Liu, W., Deng, F., Xie, S., Shen, S., Li, J.: Electromechanical analysis of direct and converse flexoelectric effects under a scanning probe tip. J. Mech. Phys. Solids **142**, 104020 (2020)
40. Yurkov, A., Yudin, P.: Continuum model for converse flexoelectricity in a thin plate. Int. J. Eng. Sci. **182**, 103771 (2023)
41. Sharma, S., Kumar, A., Kumar, R., Talha, M., Vaish, R.: Geometry independent direct and converse flexoelectric effects in functionally graded dielectrics: an isogeometric analysis. Mech. Mater. **148**, 103456 (2020)
42. Akgöz, B., Civalek, Ö.: A microstructure-dependent sinusoidal plate model based on the strain gradient elasticity theory. Acta Mech. **226**(7), 2277–2294 (2015)
43. Nye, J.F., et al.: Physical Properties of Crystals: Their Representation by Tensors and Matrices. Oxford University Press, Oxford (1985)
44. Lam, D.C., Yang, F., Chong, A., Wang, J., Tong, P.: Experiments and theory in strain gradient elasticity. J. Mech. Phys. Solids **51**(8), 1477–1508 (2003)
45. Qi, L., Zhou, S., Li, A.: Size-dependent bending of an electro-elastic bilayer nanobeam due to flexoelectricity and strain gradient elastic effect. Compos. Struct. **135**, 167–175 (2016)
46. Rupa, N.S., Ray, M.: Analysis of flexoelectric response in nanobeams using nonlocal theory of elasticity. Int. J. Mech. Mater. Des. **13**(3), 453–467 (2017)
47. Qu, Y., Zhang, G., Fan, Y., Jin, F.: A non-classical theory of elastic dielectrics incorporating couple stress and quadrupole effects: part I-reconsideration of curvature-based flexoelectricity theory. Math. Mech. Solids **26**, 1647–1659 (2021)
48. Danesh, H., Javanbakht, M.: Free vibration analysis of nonlocal nanobeams: a comparison of the one-dimensional nonlocal integral timoshenko beam theory with the two-dimensional nonlocal integral elasticity theory. Math. Mech. Solids **27**, 557–577 (2021)
49. Dehkordi, S.F., Beni, Y.T.: Electro-mechanical free vibration of single-walled piezoelectric/flexoelectric nano cones using consistent couple stress theory. Int. J. Mech. Sci. **128**, 125–139 (2017)
50. Ghobadi, A., Beni, Y.T., Golestanian, H.: Size dependent thermo-electro-mechanical nonlinear bending analysis of flexoelectric nano-plate in the presence of magnetic field. Int. J. Mech. Sci. **152**, 118–137 (2019)
51. Lee, C.K.: Theory of laminated piezoelectric plates for the design of distributed sensors/actuators. Part I: governing equations and reciprocal relationships. J. Acoust. Soc. Am. **87**(3), 1144–1158 (1990)
52. Reddy, J.N.: Mechanics of Laminated Composite Plates and Shells: Theory and Analysis. CRC Press (2004)
53. Carrera, E.: Historical review of zig-zag theories for multilayered plates and shells. Appl. Mech. Rev. **56**(3), 287–308 (2003)

54. Deng, Q., Shen, S.: The flexodynamic effect on nanoscale flexoelectric energy harvesting: a computational approach. Smart Mater. Struct. **27**(10), 105001 (2018)
55. Nguyen, B., Nanthakumar, S., Zhuang, X., Wriggers, P., Jiang, X., Rabczuk, T.: Dynamic flexoelectric effect on piezoelectric nanostructures. Eur. J. Mech. A Solids **71**, 404–409 (2018)
56. Wang, Q., Quek, S.: Flexural vibration analysis of sandwich beam coupled with piezoelectric actuator. Smart Mater. Struct. **9**(1), 103 (2000)
57. Wang, Q.: On buckling of column structures with a pair of piezoelectric layers. Eng. Struct. **24**(2), 199–205 (2002)
58. Joshan, Y.S., Santapuri, S., Grover, N.: Analysis of laminated piezoelectric composite plates using an inverse hyperbolic coupled plate theory. Appl. Math. Model. **82**, 359–378 (2020)
59. Reddy, J.N.: Energy and Variational Methods in Applied Mechanics: With an Introduction to the Finite Element Method. Wiley, New York (1984)
60. Reddy, J.N.: An Introduction to the Finite Element Method, vol. 1221. McGraw-Hill, New York (2010)
61. Babu, B., Patel, B.: On the finite element formulation for second-order strain gradient nonlocal beam theories. Mech. Adv. Mater. Struct. **26**(15), 1316–1332 (2019)
62. Deng, F., Deng, Q., Yu, W., Shen, S.: Mixed finite elements for flexoelectric solids. J. Appl. Mech. **84**(8), 081004 (2017)
63. Eliseev, E.A., Morozovska, A.N., Glinchuk, M.D., Blinc, R.: Spontaneous flexoelectric/flexomagnetic effect in nanoferroics. Phys. Rev. B **79**(16), 165433 (2009)
64. Thai, H.-T., Vo, T.P.: A size-dependent functionally graded sinusoidal plate model based on a modified couple stress theory. Compos. Struct. **96**, 376–383 (2013)
65. Meksi, R., Benyoucef, S., Mahmoudi, A., Tounsi, A., Adda Bedia, E.A., Mahmoud, S.: An analytical solution for bending, buckling and vibration responses of FGM sandwich plates. J. Sandwich Struct. Mater. **21**(2), 727–757 (2019)
66. Joshan, Y.S., Santapuri, S., Srinivasa, A.: Finite element modeling and analysis of low symmetry piezoelectric shells for design of shear sensors. Int. J. Mech. Sci. **210**, 106726 (2021)